

A refined two-scale model for Newtonian and non-Newtonian fluids in fractured poroelastic media

Tim Hageman, René de Borst*

Department of Civil and Structural Engineering, University of Sheffield, Sheffield S1 3JD, UK

Abstract

A refined model is presented which numerically resolves the fluid flow within a fracture inside a saturated poroelastic material. At the discontinuity, the mass balance of the fluid is solved using the velocity profile inside the fracture, with the velocity profile being determined numerically from the momentum balance in the integration points at the discontinuity. The resolution of the mass balance and the velocity profile in the integration points at the discontinuity is coupled to surrounding poroelastic material model in a two-scale approach. The resulting monolithic scheme allows for complex fluid behaviour to be included, which is demonstrated via the inclusion of the fluid inertia and the use of a Carreau fluid. The governing equations are discretised using T-splines, while the fracture is represented by spline-based interface elements, and an implicit time discretisation scheme is used. Mesh refinement studies are carried out for a typical case, which contains a pressurised and propagating fracture. A coarse macro-scale mesh is sufficient to obtain the correct propagation velocities, but a finer mesh is needed to prevent pressure oscillations. Time step refinement studies show the capabilities of the model to capture pressure waves within the fracture. Finally, it is shown that if inertial effects are limited and a Newtonian fluid is used, a fracture scale discretisation using a single element is sufficient. However, for a Carreau fluid or when the problem is inertia-dominated, smaller elements are needed to correctly represent the velocity profile.

Keywords: Poroelasticity, fracture, sub-grid model, isogeometric analysis, non-Newtonian fluids

1. Introduction

Simulating fracture propagation in poroelastic materials is a complex problem, requiring not only to accurately include the interaction between the interstitial fluid and the porous material, but also a physically correct description of the behaviour of the fluid inside the pressurised fracture. Recently, the effects of the fluid inertia and acceleration-driven fluid flow in the porous material were demonstrated [1]. The inclusion of these terms can cause a stick-slip like behaviour for shear fractures, whereas the fracture propagation is continuous without these terms. Similar "physics-induced" stepwise propagation has also been claimed to occur for pressurised fractures [2, 3, 4, 5]. However, the origin of the latter stepwise propagation and the accompanying pressure oscillations are unclear [6], and few finite element simulations have replicated this behaviour [7]. To study this phenomena, and to obtain more realistic results for simulations of pressurised fractures, it is interesting to include fluid inertia inside the fracture.

Currently, there exists a range of fracture flow models through which the fluid flow inside the fracture can be included [8, 9]. One of the easiest to use and most common fracture flow models is the cubic law [10, 11]. By assuming a fully developed Poiseuille flow within the fracture, this model describes the fluid flow within the fracture through an effective permeability, allowing similar equations to be used for the porous domain and the fracture itself [12, 13]. Due to the ease of use of this formulations, it has been successfully applied

*Corresponding author

Email address: `r.deborst@sheffield.ac.uk` (René de Borst)

in a large range of applications, for instance impermeable natural fractures [14] and pressurised fractures [15, 16, 17], and in methods ranging from phase-field formulations [18, 19] to extended finite element methods [20, 21]. Another way to include the fracture flow based on the cubic law is to distribute the fluid transport inside the fracture over the element in which it is contained, removing the need to separately model the fracture [22, 23, 24, 25].

While models based on the cubic law are simple to use, their disadvantage is that they cannot be used to reconstruct the behaviour of the fluid within the fracture. In contrast, methods such as the continuous pressure model [26, 27] and the discontinuous pressure model [28, 29] are directly based on analytically obtained velocity profiles within the fracture. This allows these models to reconstruct the fluid velocity within the fracture through post-processing. Due to their direct dependence on this velocity profile, complex fluid behaviour such as non-Newtonian fluids [30, 31] or multiphase fluid interactions [32, 33] can be included as long as an analytical expression for the velocity profile is available. However, an analytical expression for the velocity profile is not always available, which limits the applicability to certain fluid rheologies and prohibits the inclusion of inertial effects.

These disadvantages are removed by Direct Numerical Simulation of the flow in the interior of the fracture. This has been done using Darcy flow for the porous material, while solving the Stokes equations within the fracture [34, 35, 36], and using Brinkman flow for both the porous material and the fracture [37, 38]. Since these methods solve the fluid flow within the fracture numerically, there is no limitation on the fluid rheology or the inclusion of other physically relevant effects. However, the interior of the fracture needs to be discretised using a sufficiently fine mesh and has to be remeshed upon fracture propagation, making these methods less feasible for large-scale fracture propagation.

Herein, we describe a fracture flow model which couples a numerically resolved velocity profile to the mass conservation used in a discontinuous pressure model. This allows the advantages of a discontinuous pressure model to be retained, while partly obtaining the added advantage of directly simulating the fracture flow. The result is a scheme which does not need an analytical expression for the velocity profile, and does not need the interior of the fracture to be fully discretised. Based on previous results that inertial effects of the fluid may be physically relevant, the scheme will include these effects, resulting in a detailed description of the fluid velocity within the fracture. To show the capabilities to represent different fluid rheologies, we will derive the subgrid model for Newtonian and Carreau fluids.

In the remainder, we will first describe the governing equations for the macro scale. Next, the subgrid model for a Newtonian fluid is described, and extended to Carreau fluids in Section 4. Time and mesh refinement studies for the macro and the fracture scale meshes are carried out in Section 5. Finally, the effect of including inertial terms is given in Section 6. For completeness, the discretised equations used for the simulations are given in Appendix A.

2. Governing macro scale equations

A two-dimensional domain with a discontinuity is considered, as shown in Figure 1. The displacements in the porous material are described using a Cosserat continuum [39, 40, 41], with in two dimensions $\mathbf{u} = [u_x \ u_y \ \omega_z]^T$, u_x and u_y being the displacements, and ω_z the Cosserat microrotation. While no plasticity is used here, a Cosserat continuum allows a straightforward combination of the models used here with (non-associated) plasticity [1, 42].

For the interstitial fluid, we will adhere to the standard displacement-pressure formulation [43, 44], describing the state of the fluid through the interstitial fluid pressure p . Finally, the fracture inflow has been modelled using a discontinuous pressure model [8, 29, 45], which allows for a discontinuous pressure across the discontinuity, and features an additional degree of freedom p_d at the discontinuity which describes the fluid pressure inside the fracture.

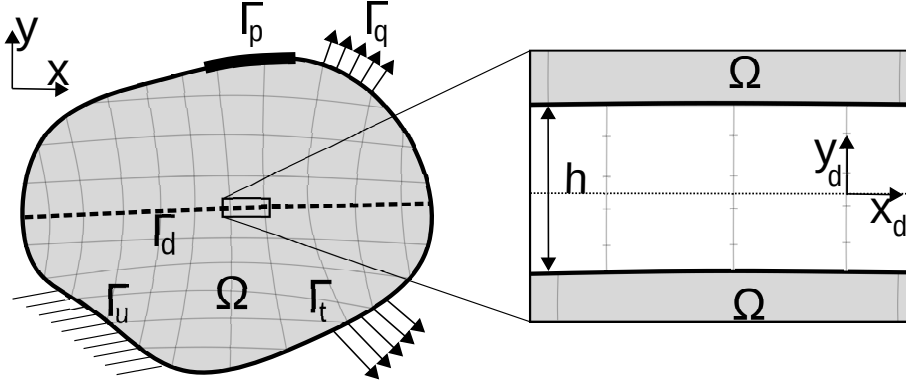


Figure 1: Overview of the fracture problem at the global and subgrid scale, including the global and the local coordinate systems

2.1. Porous medium

The porous material is described through the combined momentum balance of the solid and fluid at $t + \Delta t$:

$$\mathbf{L}^T (\boldsymbol{\sigma}_s^{t+\Delta t} - \alpha p^{t+\Delta t} \mathbf{m}) - \bar{\rho} \ddot{\mathbf{u}}^{t+\Delta t} - \rho_f \mathbf{I}_c^T \left(\frac{1}{\theta \Delta t} (\mathbf{q}^{t+\Delta t} - \mathbf{q}^t) + \left(1 - \frac{1}{\theta}\right) \dot{\mathbf{q}}^t \right) = \mathbf{0} \quad (1)$$

and the mass balance:

$$\frac{1}{M} \dot{p}^{t+\Delta t} + \alpha \nabla \cdot (\mathbf{I}_c \dot{\mathbf{u}}^{t+\Delta t}) + \nabla \cdot \mathbf{q}^{t+\Delta t} = 0 \quad (2)$$

in which a θ -scheme has been used to discretise the fluid flux terms in time. Please note that this formulation allows for the inclusion of acceleration driven fluid flow in the pressure-displacement formulation [1]. In the momentum balance, only the convective momentum transport terms ($\rho_f \mathbf{I}_c^T (\mathbf{q} \cdot \nabla) \mathbf{q}$) is neglected, whereas separate inertia terms for the solid and the fluid are retained. These equations use the volume-averaged density $\bar{\rho} = (1 - n_f) \rho_s + n_f \rho_f$, the time step size Δt , the Biot coefficient α , the Biot modulus M , and the matrices:

$$\mathbf{L}^T = \begin{bmatrix} \frac{\partial}{\partial x} & 0 & 0 & 0 & \frac{\partial}{\partial y} & 0 & 0 \\ 0 & \frac{\partial}{\partial y} & 0 & \frac{\partial}{\partial x} & 0 & 0 & 0 \\ 0 & 0 & 0 & -1 & 1 & \ell_c \frac{\partial}{\partial x} & \ell_c \frac{\partial}{\partial y} \end{bmatrix} \quad \mathbf{m} = [1 \ 1 \ 1 \ 0 \ 0 \ 0 \ 0]^T$$

$$\boldsymbol{\rho}_s = \begin{bmatrix} \rho_s & 0 & 0 \\ 0 & \rho_s & 0 \\ 0 & 0 & \Theta \end{bmatrix} \quad \boldsymbol{\rho}_f = \begin{bmatrix} \rho_f & 0 & 0 \\ 0 & \rho_f & 0 \\ 0 & 0 & 0 \end{bmatrix} \quad \mathbf{I}_c = \begin{bmatrix} 1 & 0 & 0 \\ 0 & 1 & 0 \end{bmatrix}$$

with ρ_s and ρ_f the density of the solid and the fluid respectively, ℓ_c being the Cosserat length scale, and $\Theta = 2\rho_s \ell_c^2 / (1 + \nu)$ being the rotational inertia [40]. Finally, the Darcy fluid flux term in Eqs. (1)-(2) is determined using the momentum balance of the fluid combined with Darcy's law:

$$\mathbf{q} = -\frac{k}{\mu} \left(\nabla p + \rho_f \left(\mathbf{I}_c \ddot{\mathbf{u}} + \frac{1}{n_f} \dot{\mathbf{q}} \right) \right) \quad (3)$$

Applying a θ -scheme for the time discretisation of the fluid flux at $t + \Delta t$ gives:

$$\mathbf{q}^{t+\Delta t} = \left(1 + \frac{\rho_f k}{n_f \mu \theta \Delta t} \right)^{-1} \left(-\frac{k}{\mu} \nabla p^{t+\Delta t} - \frac{k \rho_f}{\mu} \mathbf{I}_c \ddot{\mathbf{u}}^{t+\Delta t} - \frac{k \rho_f}{\mu n_f} \left(\left(1 - \frac{1}{\theta}\right) \dot{\mathbf{q}}^t - \frac{1}{\theta \Delta t} \mathbf{q}^t \right) \right) \quad (4)$$

using the intrinsic permeability k , the porosity n_f , and the fluid viscosity μ . The fluid flux \mathbf{q}^t and the change in fluid flux $\dot{\mathbf{q}}^t$ at t are used as history variables, which are updated at the end of each time step. Eq. (4) is substituted in Eqs. (1)-(2) to remove the dependence of these Equations on the fluid flux, describing the poroelastic material using a standard pressures-displacement formulation.

2.2. Discontinuity

The tractions at the discontinuity are given in a fracture-local coordinate system:

$$\boldsymbol{\tau}_d = \boldsymbol{\tau}_s - p_d \mathbf{n} \quad (5)$$

with \mathbf{n} the normal vector and $\boldsymbol{\tau}_s$ the interface traction related to the solid displacement, determined by a traction-separation law. Regarding the total interface tractions it is assumed that the shear stresses at the walls of the fracture due to fluid flow inside the fracture are small compared to the fluid pressure. This is a reasonable assumption since the shear stresses scale with the fracture opening height, whereas the normal stresses scale with the fracture length.

The description of the fluid flow at the discontinuity starts from conservation of mass in the interior of the fracture. In the local (x_d, y_d) coordinate system the later is given as:

$$\frac{\partial v}{\partial x_d} + \frac{\partial w}{\partial y_d} + \frac{1}{K_f} \dot{p}_d = 0 \quad (6)$$

using the tangential velocity v , the normal velocity w , and the bulk modulus of the fluid K_f . Integrating over the fracture height h and using the interface permeability k_i to govern the fracture flow at the walls results in:

$$k_i \left(p^{+t+\Delta t} + p^{-t+\Delta t} - 2p_d^{t+\Delta t} \right) + \frac{\partial}{\partial x} q_x + \dot{h}^{t+\Delta t} + \frac{h}{K_f} \dot{p}_d^{t+\Delta t} = 0 \quad (7)$$

in which the fracture height h is given by:

$$h = h_0 + \mathbf{n} \cdot \llbracket \mathbf{u} \rrbracket \quad (8)$$

using the displacement jump $\llbracket \mathbf{u} \rrbracket$ and the normal vector \mathbf{n} . q_x is the fluid flux inside the fracture, obtained through the subgrid model. The term h_0 introduces an offset to the fracture opening height, which can be used to impose an initial fracture opening height without actually requiring the opening height to be reflected in the spatial discretisation or the initial deformation state of the domain. Initial opening heights are often encountered in pre-existing fractures or when using notched specimens to trigger propagation at a set location [6, 46, 47, 48, 49].

The temporal discretisation has been carried out using a combination of a θ -scheme for the interstitial pressure and the discontinuity pressure, and a Newmark scheme for the displacements. The spatial discretisation using T-splines [50, 51] is cast into a traditional finite element framework using Bézier extraction [52, 53]. The discontinuity is included using isogeometric interface elements [54, 55, 56, 57], and propagated along a C^0 continuity line to remove the need for remeshing upon fracture propagation [42], see Appendix A for details on the discretisation. It is noted that although T-splines are used for the discretisation, the subgrid model described in the next section is independent of the spatial discretisation method used for the macro scale and is applicable in conjunction with any discretisation method.

3. Fracture subgrid model

The fluid flux q_x is computed using a separate model for flow in the fracture. It gives the fluid flux as a function of the current fracture opening height h and the pressure gradient $\partial p_d / \partial x_d$. For this subgrid model to be fully integrated in the macro-scale formulation, and to preserve quadratic converging [58], the derivative of q_x with regard to the pressure gradient and the fracture opening height are also needed.

To obtain the fluid flux within the fracture, we start with the momentum balance in the x_d -direction:

$$\rho_f \frac{\partial v}{\partial t} + \rho_f v \frac{\partial v}{\partial x_d} + \rho_f w \frac{\partial v}{\partial y_d} = - \frac{\partial p_d}{\partial x_d} + \mu \frac{\partial^2 v}{\partial y_d^2} \quad (9)$$

assuming a no-slip condition at the walls of the fracture:

$$v(h/2) = v(-h/2) = 0 \quad (10)$$

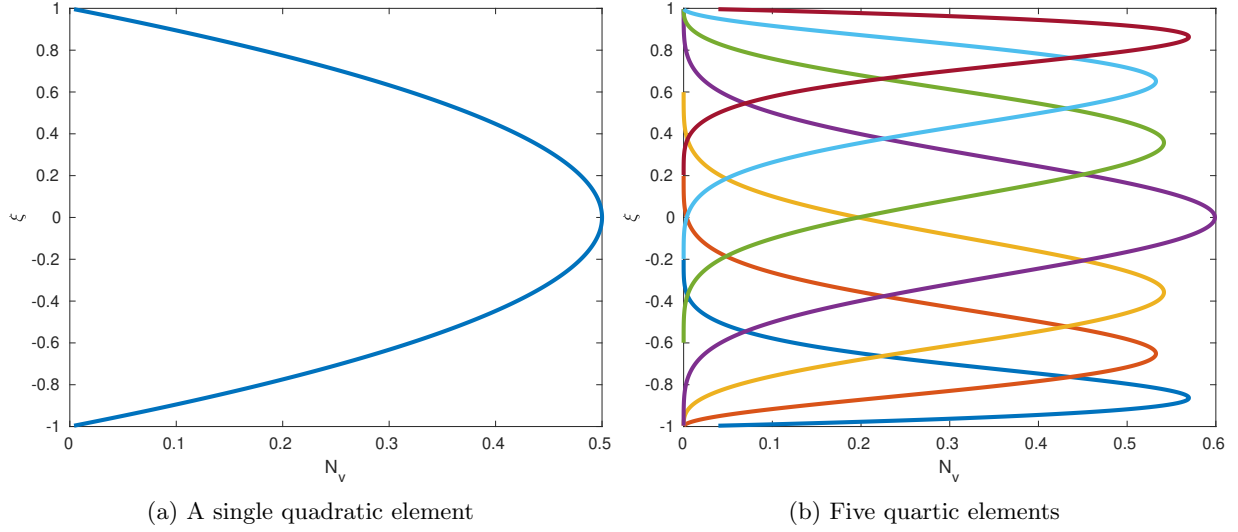


Figure 2: Examples of the interpolants used for the velocity profile discretisation.

To keep the formulation localised within an integration point, we assume the effects of convective momentum transport (the terms $\rho_f v \frac{\partial v}{\partial x_d}$ and $\rho_f w \frac{\partial v}{\partial y_d}$) to be small compared to the viscosity and pressure-related terms. Furthermore, since the fracture has a small opening height, we can assume the flow to locally be one-dimensional in the x_d -direction, with the vertical flux obtained through the macro-scale mass conservation from Eq. (7).

The time derivative of the velocity inside the fracture is discretised in the same manner as the fluid flux inside the porous material, i.e. using a θ -scheme:

$$\frac{\partial v}{\partial t} = \frac{1}{\theta \Delta t} (v^{t+\Delta t} - v^t) + (1 - \frac{1}{\theta}) \dot{v}^t \quad (11)$$

which allows the horizontal momentum balance to be discretised in time as follows:

$$\rho_f \left(\frac{1}{\theta \Delta t} (v^{t+\Delta t} - v^t) + (1 - \frac{1}{\theta}) \dot{v}^t \right) + \frac{\partial p_d}{\partial x} - \mu \frac{\partial^2 v^{t+\Delta t}}{\partial y^2} = 0 \quad (12)$$

Since the velocity depends on the history of the velocity, v^t and \dot{v}^t , it is not possible to obtain an explicit expression for the velocity profile as was done in [26]. Instead, the velocity profile at the integration point is represented through Bézier extracted NURBS \mathbf{N}_v^{el} in a standard finite element format as:

$$v = \sum_{el}^{n_{el}} \mathbf{N}_v^{el} \mathbf{v}^{el} \quad (13)$$

with the total height of these elements being defined in parametric (ξ, v) space to remove the dependence of the discretisation on the fracture opening height. The parametric coordinate ξ is mapped to the local coordinate through a linear mapping $y_d = h/2 \xi$. Since the discretisation itself is independent of the opening height of the fracture, the same discretisation can be used to determine the fluid flux in *all* the integration points at the macro-scale. The no-slip boundary conditions are directly imposed by removing the non-zero spline at the top and bottom, as shown in Figure 2. This discretisation is used for the new and old velocity, as well as for its time derivative at t . It is emphasised that, while NURBS are used for the discretisation to obtain a smooth velocity profile, the discretisation could also have been done using Lagrangian-based interpolants.

Using the discretisation from Eq. (13), the weak form of the momentum balance is given by:

$$\frac{h}{2} \int_{-1}^1 \rho_f \mathbf{N}_v^T \left(\frac{1}{\theta \Delta t} (\mathbf{N}_v \mathbf{v}^{t+\Delta t} - \mathbf{N}_v \mathbf{v}^t) + (1 - \frac{1}{\theta}) \mathbf{N}_v \dot{\mathbf{v}}^t \right) + \mathbf{N}_v^T \frac{\partial p_d}{\partial x_d} - \frac{4\mu}{h^2} \left(\frac{\partial \mathbf{N}_v}{\partial \xi} \right)^T \frac{\partial \mathbf{N}_v}{\partial \xi} \mathbf{v}^{t+\Delta t} d\xi = 0 \quad (14)$$

which can be rewritten as:

$$\frac{\rho_f h^2}{4\mu} \mathbf{C} \left(\frac{1}{\theta \Delta t} \mathbf{v}^{t+\Delta t} - \frac{1}{\theta \Delta t} \mathbf{v}^t + \left(1 - \frac{1}{\theta}\right) \dot{\mathbf{v}}^t \right) + \frac{h^2}{4\mu} \frac{\partial p_d}{\partial x_d} \mathbf{w} + \mathbf{D} \mathbf{v}^{t+\Delta t} = \mathbf{0} \quad (15)$$

using the definitions:

$$\mathbf{C} = \int_{-1}^1 \mathbf{N}_v^T \mathbf{N}_v d\xi \quad (16)$$

$$\mathbf{D} = \int_{-1}^1 \left(\frac{\partial \mathbf{N}_v}{\partial \xi} \right)^T \frac{\partial \mathbf{N}_v}{\partial \xi} d\xi \quad (17)$$

$$\mathbf{w} = \int_{-1}^1 \mathbf{N}_v^T d\xi \quad (18)$$

These matrices are constant throughout the simulation and independent of the integration point. Therefore, they only need to be calculated once and can thereafter be used to obtain the velocity for all the integration points. This results in an explicit expression for the velocity, solely dependent on the macro-scale degrees of freedom and on the history variables at the subgrid (fracture) scale:

$$\mathbf{v}^{t+\Delta t} = \mathbf{Q}^{-1} \left(\frac{\rho_f h^2}{4\mu} \mathbf{C} \left(\frac{1}{\theta \Delta t} \mathbf{v}^t - \left(1 - \frac{1}{\theta}\right) \dot{\mathbf{v}}^t \right) - \frac{h^2}{4\mu} \frac{\partial p_d}{\partial x_d} \mathbf{w} \right) \quad (19)$$

with:

$$\mathbf{Q} = \frac{\rho_f h^2}{4\mu \theta \Delta t} \mathbf{C} + \mathbf{D} \quad (20)$$

Finally, the velocity profile is integrated over the fracture height to obtain the flux term required for the integration of the interface element:

$$q_x = \frac{h}{2} \mathbf{w}^T \mathbf{v}^{t+\Delta t} = \mathbf{w}^T \mathbf{Q}^{-1} \left(\frac{\rho_f h^3}{8\mu} \mathbf{C} \left(\frac{1}{\theta \Delta t} \mathbf{v}^t - \left(1 - \frac{1}{\theta}\right) \dot{\mathbf{v}}^t \right) - \frac{h^3}{8\mu} \frac{\partial p_d}{\partial x_d} \mathbf{w} \right) \quad (21)$$

This fluid flux is used in the macro-scale formulation of Eq. (7), which gives the coupling between the velocity profiles determined in each integration point on the discontinuity and the interstitial pressures within the porous material.

If the velocity profile is approximated using a single quadratic interpolant (the velocity profile when negligible effects of inertia are present), this identity reduces to ($\mathbf{C} = 4/15 \mathbf{I}$, $\mathbf{D} = 2/3 \mathbf{I}$, $\mathbf{w}^T = 2/3 \mathbf{i}$ with \mathbf{I} the 1×1 identity matrix and \mathbf{i} an array filled with 1):

$$q_x = \left(\frac{\rho_f h^2}{10\mu \Delta t} + 1 \right)^{-1} \left(\frac{\rho_f h^3}{30\mu} \left(\frac{1}{\theta \Delta t} \mathbf{v}^t - \left(1 - \frac{1}{\theta}\right) \dot{\mathbf{v}}^t \right) - \frac{h^3}{12\mu} \frac{\partial p_d}{\partial x_d} \right)$$

which, in the case of negligible inertia ($\rho_f = 0$) reduces to the cubic law, $q_x = -\frac{h^3}{12\mu} \frac{\partial p_d}{\partial x_d}$.

The derivatives of Eq. 21 with regard to h and $\partial p_d / \partial x_d$ are required for the global tangential matrices, see also Eqs (A.20)-(A.21). They read:

$$\frac{\partial q_x}{\partial \frac{\partial p_d}{\partial x_d}} = -\frac{h^3}{8\mu} \mathbf{w}^T \mathbf{Q}^{-1} \mathbf{w} \quad (22)$$

and

$$\begin{aligned} \frac{\partial q_x}{\partial h} = & \mathbf{w}^T \mathbf{Q}^{-1} \left(\frac{3\rho_f h^2}{8\mu} \mathbf{C} \left(\frac{1}{\theta \Delta t} \mathbf{v}^t - \left(1 - \frac{1}{\theta}\right) \dot{\mathbf{v}}^t \right) - \frac{3h^2}{8\mu} \frac{\partial p_d}{\partial x_d} \mathbf{w} \right) \\ & - \mathbf{w}^T \mathbf{Q}^{-1} \left(\frac{\rho_f h}{2\mu \theta \Delta t} \mathbf{C} \right) \mathbf{Q}^{-1} \left(\frac{\rho_f h^3}{8\mu} \mathbf{C} \left(\frac{1}{\theta \Delta t} \mathbf{v}^t - \left(1 - \frac{1}{\theta}\right) \dot{\mathbf{v}}^t \right) - \frac{h^3}{8\mu} \frac{\partial p_d}{\partial x_d} \mathbf{w} \right) \end{aligned} \quad (23)$$

110 These derivatives allow the subgrid (fracture scale) model to be fully integrated in a monolithic scheme formulated at the macro scale, resulting in an optimal (quadratic) convergence rate for a Newton-Raphson scheme.

4. Extension to non-Newtonian fluids

The ability of the model to represent more complex fluids will now be demonstrated at the hand of a Carreau fluid [59]. In this model the effective viscosity is a function of the shear rate $\dot{\gamma}$, as follows:

$$\mu_{eff} = \mu_{\infty} + (\mu_0 - \mu_{\infty}) (1 + a_c^2 \dot{\gamma}^2)^{(n-1)/2} \quad (24)$$

with n being the non-Newtonian fluid index, where $n < 1$ for shear-thinning fluids and $n = 1$ for Newtonian fluids. Different from other non-Newtonian fluids, for instance the power-law fluid model, a Carreau fluid introduces an upper and a lower limit for the effective viscosity at low and high shear rates, μ_0 and μ_{∞} , respectively, and transitions smoothly between these limit values. This smooth transition is preferable to avoid convergence issues that can occur for non-smooth functions. The factor a_c indicates when the transition from μ_0 starts, with higher values for a_c delaying this transition until a higher shear rate is achieved. The shear rate $\dot{\gamma}$ is defined within the fracture as $\dot{\gamma} = \partial v / \partial y_d$, and approximated inside the porous material as $\dot{\gamma} = |\mathbf{q}| / (c\sqrt{k})$ [60, 61, 62] with the coefficient c a factor which represents the small-scale geometry of the porous material.

4.1. Porous medium & discontinuity

The discretised balances of mass and momentum in the porous material, Eqs (2) and (1), and the mass conservation at the discontinuity, Eq. (7), continue to be valid for non-Newtonian fluids. The only difference in the description of the porous medium is the expression for $\mathbf{q}^{t+\Delta t}$, which, instead of Eq. (4), is now given by:

$$\begin{aligned} -\nabla p^{t+\Delta t} - \rho_f \mathbf{I}_c \ddot{\mathbf{u}}^{t+\Delta t} + \frac{\rho_f}{n_f \theta \Delta t} \mathbf{q}^t - \frac{\rho_f}{n_f} \left(1 - \frac{1}{\theta}\right) \dot{\mathbf{q}}^t = \\ \left(\frac{\mu_0 - \mu_{\infty}}{k} \left(1 + \frac{a_c^2}{c^2 k} (\mathbf{q}^{t+\Delta t})^T \mathbf{q}^{t+\Delta t}\right)^{\frac{n-1}{2}} + \frac{\mu_{\infty}}{k} + \frac{\rho_f}{n_f \theta \Delta t} \right) \mathbf{q}^{t+\Delta t} \end{aligned} \quad (25)$$

The discretised form of this identity and the iterative procedure to obtain the new fluid flux $\mathbf{q}^{t+\Delta t}$ are given in Appendix A.1.

4.2. Fracture scale model

For a Carreau fluid the momentum balance in the x_d -direction is given by:

$$\frac{\rho_f}{\theta \Delta t} (v^{t+\Delta t} - v^t) + \rho_f \left(1 - \frac{1}{\theta}\right) \dot{v}^t + \frac{\partial p_d^{t+\Delta t}}{\partial x_d} - \frac{\partial}{\partial y} \left(\left(\mu_{\infty} + (\mu_0 - \mu_{\infty}) \left(1 + a_c^2 \left(\frac{\partial v^{t+\Delta t}}{\partial y_d}\right)^2\right)^{\frac{n-1}{2}} \right) \frac{\partial v^{t+\Delta t}}{\partial y_d} \right) = 0 \quad (26)$$

After discretisation this can be written in a form similar to Eq. (15):

$$\frac{\rho_f h^2}{4\mu_{\infty}} \mathbf{C} \left(\frac{1}{\theta \Delta t} \mathbf{v}^{t+\Delta t} - \frac{1}{\theta \Delta t} \mathbf{v}^t + \left(1 - \frac{1}{\theta}\right) \dot{\mathbf{v}}^t \right) + \frac{h^2}{4\mu_{\infty}} \frac{\partial p_d}{\partial x} \mathbf{w} + \left(\mathbf{D} + \frac{\mu_0 - \mu_{\infty}}{\mu_{\infty}} \mathbf{D}_{nn} \right) \mathbf{v}^{t+\Delta t} = \mathbf{0} \quad (27)$$

with \mathbf{C} , \mathbf{D} , and \mathbf{w} as in Eqs. (16)-(18). The additional, non-linear term representing the behaviour of the Carreau fluid, is given by:

$$\mathbf{D}_{nn} = \int_{-1}^1 \left(\frac{\partial \mathbf{N}_v}{\partial \xi} \right)^T \left(1 + \frac{4a_c^2}{h^2} \left(\frac{\partial \mathbf{N}_v}{\partial \xi} \mathbf{v}^{t+\Delta t} \right)^2 \right)^{\frac{n-1}{2}} \frac{\partial \mathbf{N}_v}{\partial \xi} d\xi \quad (28)$$

This equation is solved iteratively to obtain the fluid velocity associated with the control points using:

$$\mathbf{Q}_{nn} \Delta \mathbf{v}_{j+1}^{t+\Delta t} = -\frac{\rho_f h^2}{4\mu_{\infty}} \mathbf{C} \left(\frac{1}{\theta \Delta t} \mathbf{v}_j^{t+\Delta t} - \frac{1}{\theta \Delta t} \mathbf{v}^t + \left(1 - \frac{1}{\theta}\right) \dot{\mathbf{v}}^t \right) - \frac{h^2}{4\mu_{\infty}} \frac{\partial p_d}{\partial x_d} \mathbf{w} - \left(\mathbf{D} + \frac{\mu_0 - \mu_{\infty}}{\mu_{\infty}} \mathbf{D}_{nnj} \right) \mathbf{v}_j^{t+\Delta t} \quad (29)$$

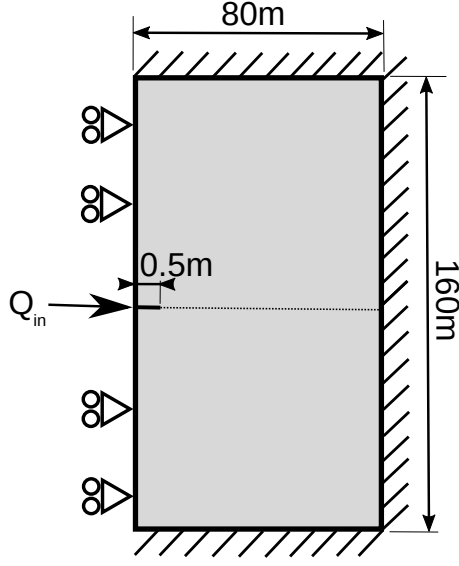


Figure 3: Geometry and boundary conditions.

with the tangential matrix given by:

$$\mathbf{Q}_{nn} = \left(\frac{\rho_f h^2}{4\mu_\infty \theta \Delta t} \mathbf{C} + \mathbf{D} + \frac{\mu_0 - \mu_\infty}{\mu_\infty} \frac{\partial \mathbf{D}_{nn} \mathbf{v}^{t+\Delta t}}{\partial \mathbf{v}^{t+\Delta t}} \right) \quad (30)$$

where:

$$\frac{\partial \mathbf{D}_{nn} \mathbf{v}^{t+\Delta t}}{\partial \mathbf{v}^{t+\Delta t}} = \mathbf{D}_{nn} + \int_{-1}^1 \frac{4a_c^2(n-1)}{h^2} \left(1 + \frac{4a_c^2}{h^2} \left(\frac{\partial \mathbf{N}_v}{\partial \xi} \mathbf{v}^{t+\Delta t} \right)^2 \right)^{\frac{n-3}{2}} \left(\frac{\partial \mathbf{N}_v}{\partial \xi} \mathbf{v}^{t+\Delta t} \right)^2 \left(\frac{\partial \mathbf{N}_v}{\partial \xi} \right)^T \frac{\partial \mathbf{N}_v}{\partial \xi} d\xi \quad (31)$$

Once a converged velocity profile has been obtained, the profile is integrated over the fracture height using Eq. (21) and coupled to the macro-scale models through Eq. (7). The derivatives of these equations (for use in the monolithic solver) are given as:

$$\frac{\partial q_x}{\partial \frac{\partial p_d^{t+\Delta t}}{\partial x_d}} = -\frac{h^3}{8\mu_\infty} \mathbf{w}^T \mathbf{Q}_{nn}^{-1} \mathbf{w} \quad (32)$$

$$\begin{aligned} \frac{\partial q_x}{\partial h} = & \frac{1}{2} \mathbf{w}^T \mathbf{v}^{t+\Delta t} - \frac{h}{2} \mathbf{w}^T \mathbf{Q}_{nn}^{-1} \left(\frac{2\rho_f h}{4\mu_\infty} \mathbf{C} \left(\frac{1}{\theta \Delta t} \mathbf{v}^{t+\Delta t} - \frac{1}{\theta \Delta t} \mathbf{v}^t + \left(1 - \frac{1}{\theta}\right) \dot{\mathbf{v}}^t \right) \right. \\ & \left. + \frac{2h}{4\mu_\infty} \frac{\partial p_d^{t+\Delta t}}{\partial x_d} \mathbf{w} + \frac{\mu_0 - \mu_\infty}{\mu_\infty} \frac{\partial \mathbf{D}_{nn} \mathbf{v}^{t+\Delta t}}{\partial h} \right) \end{aligned} \quad (33)$$

with

$$\frac{\partial \mathbf{D}_{nn}}{\partial h} = -\frac{4a_c^2(n-1)}{h^3} \int_{-1}^1 \left(\frac{\partial \mathbf{N}_v}{\partial \xi} \right)^T \left(1 + \frac{4a_c^2}{h^2} \left(\frac{\partial \mathbf{N}_v}{\partial \xi} \mathbf{v}^{t+\Delta t} \right)^2 \right)^{\frac{n-3}{2}} \left(\frac{\partial \mathbf{N}_v}{\partial \xi} \mathbf{v}^{t+\Delta t} \right)^2 \frac{\partial \mathbf{N}_v}{\partial \xi} d\xi \quad (34)$$

the derivative of the nonlinear diffusion matrix with respect to the height h .

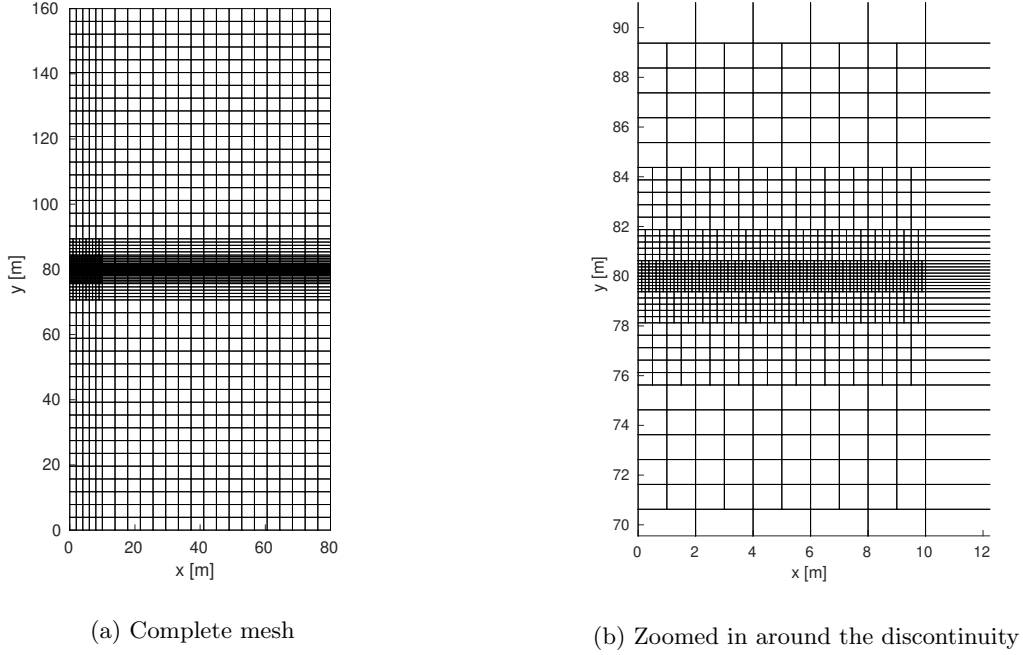
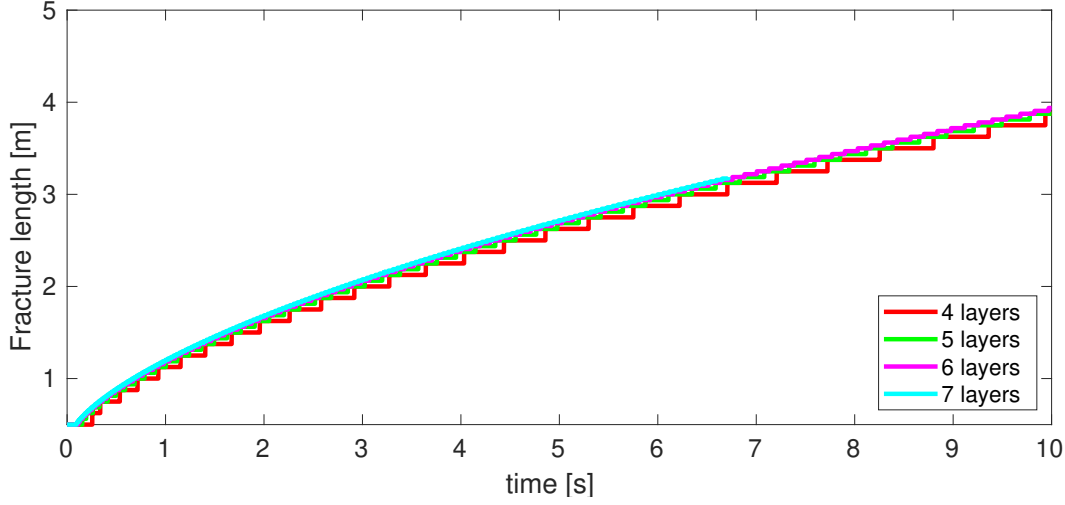


Figure 4: Mesh used for the mesh refinement study (4 layers of refinement).

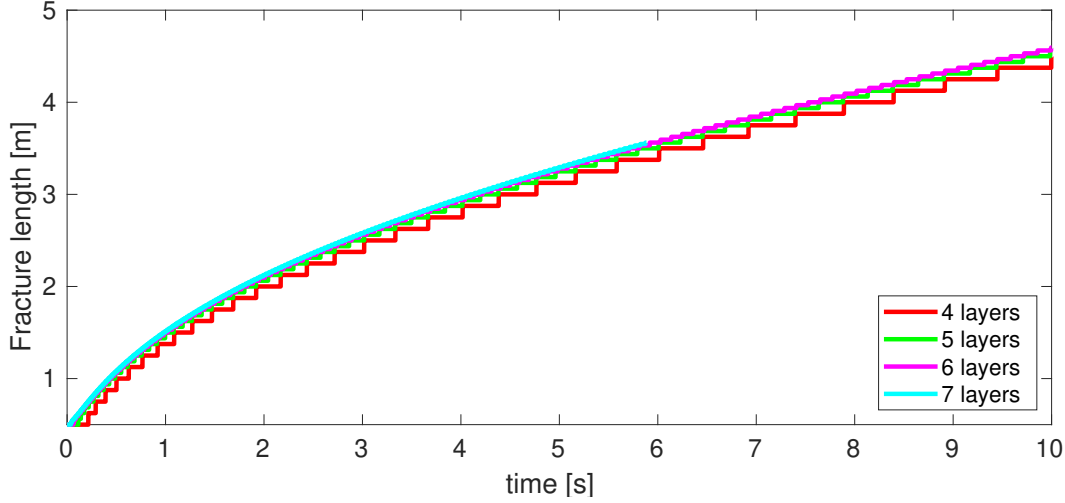
5. Mesh and time step sensitivity

A typical case is now considered [2, 49], consisting of a 80×160 m domain with an initial 0.5 m horizontal fracture, shown in Figure 3. This fracture has an initial opening height $h_0 = 0.05$ mm, with the discontinuous solid interpolants used to set this initial opening height for the larger part of the initial fracture, and smoothly becoming zero at the fracture tip to avoid issues relating to a jump in the fracture opening height between elements. The solid is characterised by a Young's modulus $E = 15$ GPa, a Poisson ratio $\nu = 0.2$, a density $\rho_s = 2500$ kg/m³, a Cosserat length scale $\ell_c = 10$ mm, a Cosserat shear modulus $G_c = 4$ GPa, an intrinsic permeability $k = 10^{-14}$ m², a porosity $n_f = 0.2$, a Biot coefficient $\alpha = 1.0$, and a bulk modulus $K_s = 30$ GPa. A (water-like) Newtonian fluid with viscosity $\mu = 1$ mPa · s, fluid density $\rho_f = 1000$ kg/m³, and bulk modulus $K_f = 1$ GPa has been used, as well as a shear-thinning Carreau fluid with $n = 0.6$, $\mu_0 = 10^3$ mPa · s, $\mu_\infty = 10^{-3}$ mPa · s, $a_c = 10^8$ s and $c = 1.0$. At the discontinuity the interface permeability $k_i = 10^{-10}$ m/Pa · s has been used, and the normal traction for fractured elements is derived from an exponential traction-separation law, with a tensile strength $f_t = 0.1$ MPa and fracture energy $\mathcal{G}_f = 0.1$ kN/m. The temporal discretisation used $\beta = 0.4$, $\gamma = 0.75$, $\theta = 1.0$, resulting in an implicit Euler scheme for the interstitial and discontinuity pressures, and a Newmark scheme with added damping for the displacements.

The coarsest mesh of the mesh refinement study is shown in Figure 4. The smallest elements have an element size $dx = dy = 0.125$ m near the interface, with larger elements further away from the discontinuity resulting in 4 layers of refinement. For the finer meshes additional refinements are added near the discontinuity, resulting in a 5-layer mesh ($dx = 62.5$ mm), a 6-layer mesh ($dx = 31.25$ mm), and a 7-layer mesh ($dx = 15.625$ mm). To facilitate remeshing due to fracture propagation, a C^0 continuity line is inserted ahead of the initial fracture and the crack is only allowed to propagate along this line. A time refinement study has been carried out using time step sizes $\Delta t = 100$ ms, $\Delta t = 10$ ms, $\Delta t = 1$ ms, $\Delta t = 0.1$ ms, and $\Delta t = 0.01$ ms. Finally, the mesh refinement study at the fracture scale discretises the fracture height using 2 linear elements (Figure 11a), 1 quadratic element (Figure 2a), 1 quartic element (Figure 11b), 5 quartic elements (Figure 2b), and 20 quartic elements (Figure 11c). All simulations have been performed for a total



(a) Newtonian fluid



(b) Carreau fluid ($n=0.6$)

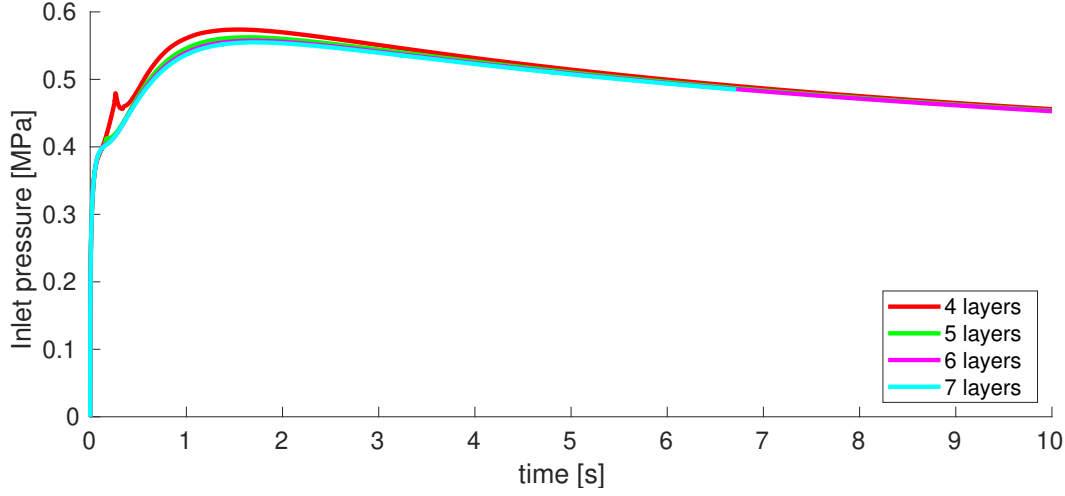
Figure 5: Fracture length resulting from mesh refinement using $\Delta t = 1$ ms

time span of 10 s, except for of the cases using $\Delta t = 0.1$ ms, $\Delta t = 0.01$ ms, and the 7-layer mesh, which were only simulated up to the point where they coincided with the results from simulations using coarser time steps or meshes.

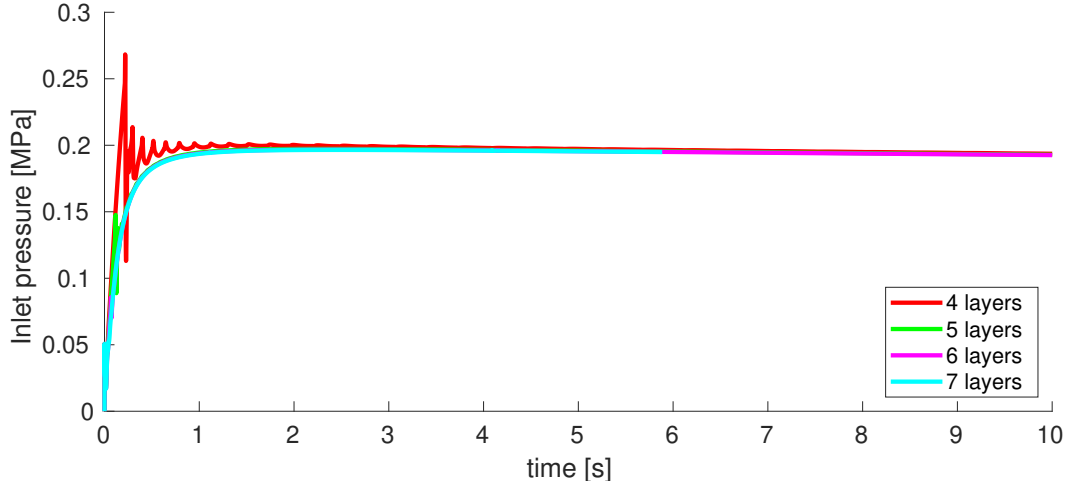
5.1. Mesh refinement

The mesh refinement study uses $\Delta t = 1$ ms and 20 quartic elements in the subgrid model for the discretisation of the height of the fracture. The computed fracture propagation is shown in Figure 5. Small propagation steps are observed for all meshes, which is caused by the combination of a small time step and the element-wise propagation associated with the use of interface elements. While the magnitude of these steps decreases upon mesh refinement, they are still present for the finest mesh since either no element or only one element fractures within a single time step for these small time steps. This stepwise propagation does not influence the overall fracturing behaviour, and only small differences are observed between the different meshes.

However, large differences are observed for the pressure inside the discontinuity at the inlet, see Figure



(a) Newtonian fluid



(b) Carreau fluid ($n=0.6$)

Figure 6: Discontinuity pressure at the inlet ($x = 0$) resulting from mesh refinement using $\Delta t = 1$ ms

6. For the 4-layer mesh, large pressure oscillations occur for the shear-thinning fluid, with the peaks of these oscillations within 2-3 time steps from the fracture propagating. A single small oscillation occurs for the Newtonian fluid, corresponding to the onset of fracture propagation. Upon mesh refinement, these oscillations disappear for the Newtonian fluid, and strongly reduce for the Carreau fluid. This suggests that the pressure oscillations are caused by the sudden increase in fracture length and the accompanying sudden increase in volume inside the fracture, and therefore disappear once smaller elements are used.

5.2. Time step refinement

Motivated by the results of the previous subsection, a time step refinement has been carried out using the 6-layer mesh. This mesh has been shown to be sufficiently fine to resolve the fracture propagation and the spike in the pressure. The time step size did not alter the fracture propagation, with the same fracture length after 10 seconds for all time steps, both for the Newtonian and the Carreau fluids (not shown).

The influence of the time step size on the inlet pressure is shown in Figure 7. For the Newtonian fluid only small differences are seen between the two largest time step sizes, and smaller time steps do not alter the computed pressures. However, the Carreau fluid shows pressure oscillations, which increase upon refinement

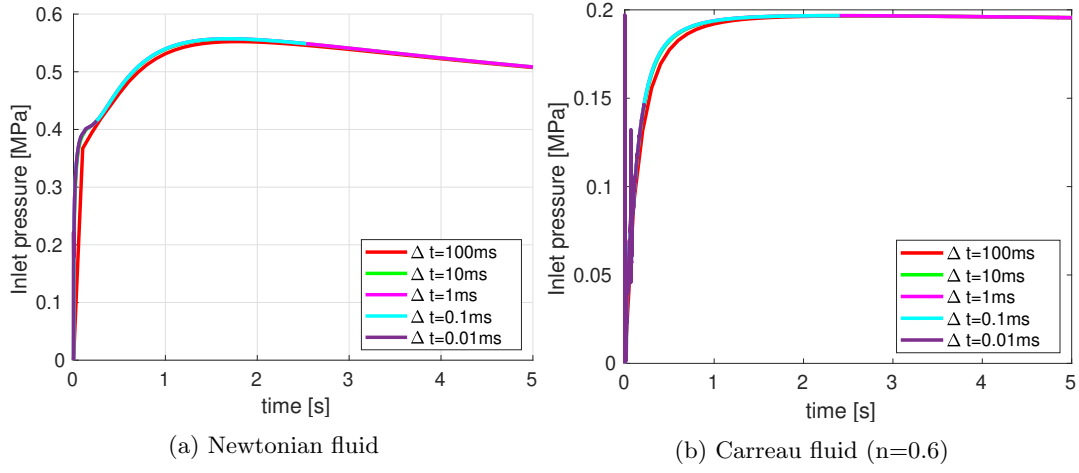


Figure 7: Pressure in the discontinuity at the inlet ($x = 0$) using the 6-layer mesh

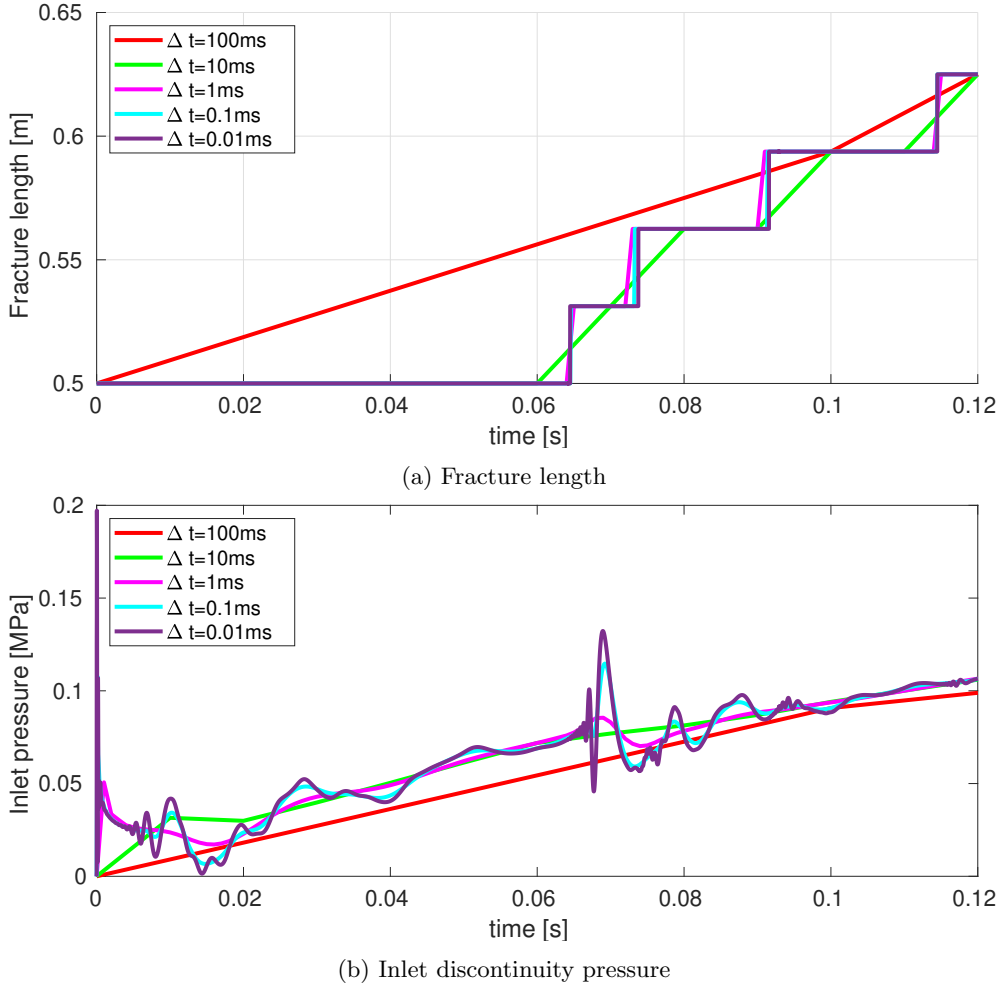


Figure 8: Pressure in the discontinuity and fracture length using the 6-layer mesh for a Carreau fluid ($n=0.6$) at the onset of the simulations

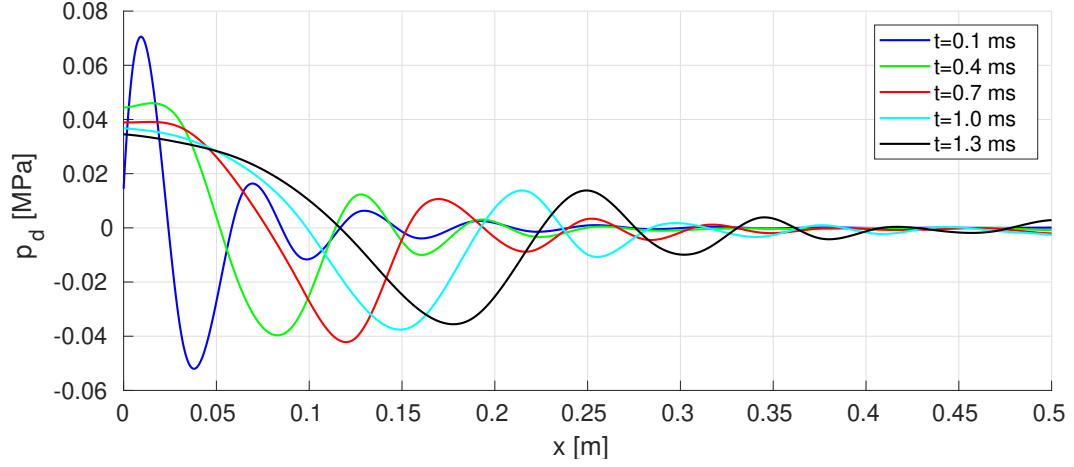


Figure 9: Pressure inside the discontinuity using the 6-layer mesh and $\Delta t = 0.01$ ms at the onset of the simulation

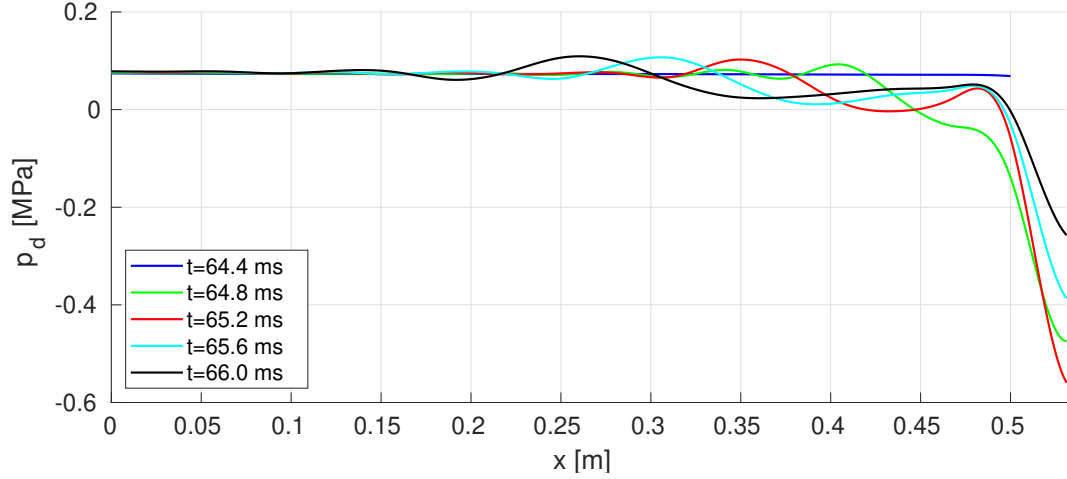


Figure 10: Pressure inside the discontinuity using the 6-layer mesh and $\Delta t = 0.01$ ms around the moment of fracture propagation

of the time step. These oscillations correspond to the onset of the simulation and the first few propagation steps, as shown in Figure 8, and originate from the element-wise fracture propagation and initial conditions.

The oscillations which originate from the initial conditions are shown in Figure 9 for the complete discontinuity. Starting from the initial condition $p_d = 0$, the pressure quickly increases at the inlet to overcome the fluid inertia. The pressure decreases once the fluid starts moving and inertial effects are less relevant. This creates a pressure peak which travels through the fracture, while decreasing in magnitude due to fluid diffusion and numerical damping. It is noted that we observe smaller oscillations ahead of this pressure peak. They are most likely caused by the sharp pressure gradients and the inability of the discretisation to properly resolve the steep gradients. Due to the inclusion of the fluid inertia, these oscillations travel along the discontinuity, while dissipating slowly.

Similar pressure oscillations occur upon fracture propagation, as shown in Figure 10. The extra length and volume which is suddenly created by the extending fracture causes a large drop in pressure at the fracture tip, while sending a pressure wave towards the inlet. However, this sudden pressure drop is an effect of the element-wise fracture propagation method, and is unlikely to occur with a continuous and smooth propagation velocity.

While some of these pressure oscillations are caused by the element-wise fracture propagation, they show the magnitude of pressure oscillations that can occur inside the fracture due to initial conditions or sudden

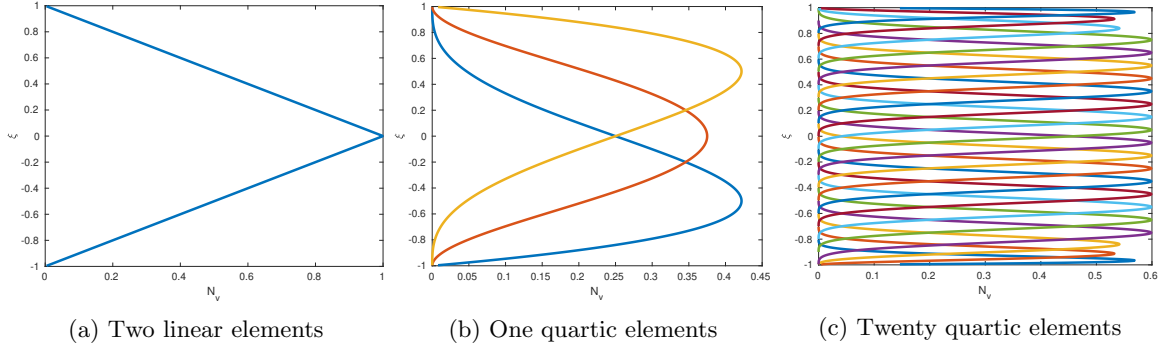


Figure 11: Discretisation used for the fracture height

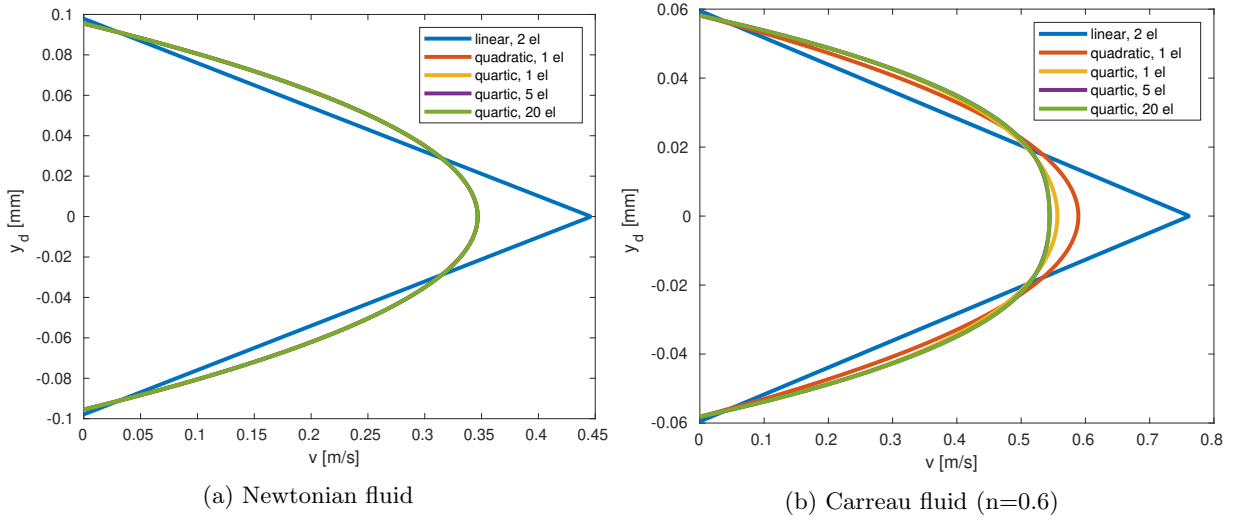


Figure 12: Fluid velocity profile at $x = 0.25$ m, $t = 5$ s

changes in the volume within the fracture. Even though the sub-grid model interacts solely through the discontinuity pressure with the other integration points at the macro-scale, this coupling appears sufficient to simulate propagating waves. These oscillations span multiple time steps and persist upon refinement of the time step, indicating that even though their origin may not be physically correct, their behaviour, once created, is.

5.3. Sensitivity to mesh refinement at the fracture scale

We now analyse the effect of the discretisation used for the subgrid model. The 6-layer mesh with $\Delta t = 1$ ms is used for all simulations, while for the subgrid model the following discretisations have been employed: 2 linear elements (Figure 11a), 1 quadratic element (Figure 2a), 1 quartic element (Figure 11b), 5 quartic elements (Figure 2b), and 20 quartic elements (Figure 11c).

The velocity profile inside the fracture at $x = 0.25$ m is shown in Figure 12a for a Newtonian fluid. Since the effects of inertia are negligible, the velocity profile can be represented exactly using a single quadratic polynomial and all discretisations therefore correspond to this solution, except for the linear discretisation. Also the pressure in the discontinuity, Figure 13a, therefore coincide, except for that resulting from the linear discretisation. Based on this velocity profile, the shear stress at the wall is calculated as $\tau_f = \mu \partial v / \partial y_d = 8$ Pa. Since this is several orders of magnitude lower than the stress that derives from the traction-separation law and the fluid pressure, which are both $\mathcal{O}(\text{MPa})$, the assumption made in Section 2.2 to neglect the fluid shear stress on the wall is justified.

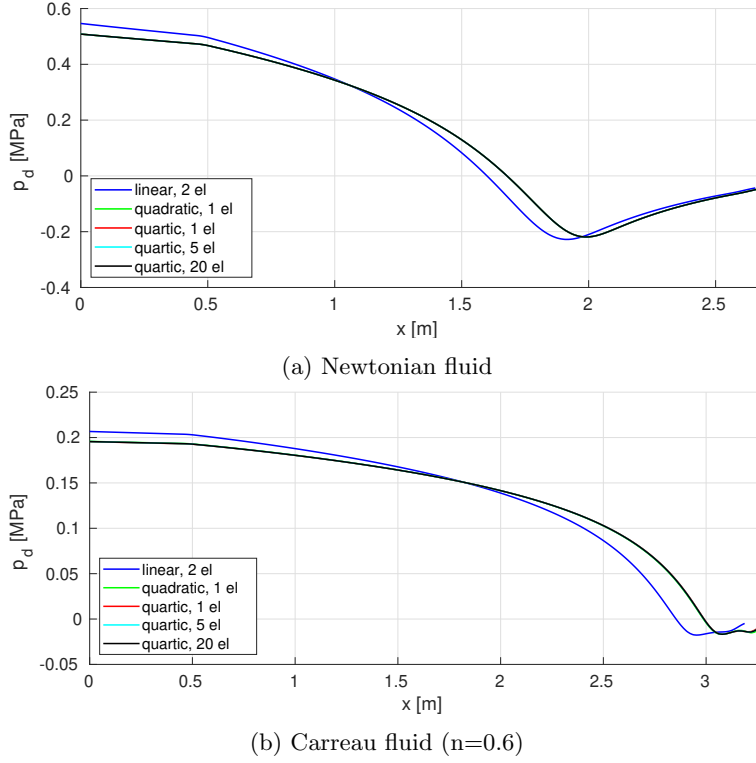


Figure 13: Discontinuity pressure at $t = 5$ s

The velocity profile for a Carreau fluid is no longer a parabola and therefore small differences are seen between the quadratic and quartic discretisations, Figure 12b. Small differences also occur between the discretisations with a single and with five quartic elements, but there is no difference anymore between the five and twenty element discretisations. However, the effects of the discretisation on the pressure in the discontinuity is similar as for Newtonian fluids, as shown in Figure 13b. There is a difference in velocity profile, but the effect on the pressure is limited due to the integration over the height. This indicates that an approximation of the velocity profile is sufficient to accurately include the effects of the fracture flow on the macro-scale system, while a finer subgrid scale discretisation is needed to obtain correct velocity profiles within the fracture when inertial effects are negligible.

6. Effect of inertia: Initial opening height h_0

We now study the importance of the fluid inertia for a Newtonian fluid by varying the initial opening height between $h_0 = 0$ mm, $h_0 = 0.05$ mm, $h_0 = 0.5$ mm, and $h_0 = 5$ mm. Since the response time of the fluid approximately scales with $\rho_f h^2 / \mu$, these opening height cover the whole range between no influence of inertia to inertia-dominated fracture flow. As in the previous section, the 6-layer mesh is used for the spatial discretisation with $\Delta t = 1$ ms, and the velocity profile inside the discontinuity is resolved using 20 quartic elements.

The development of the velocity profile inside the discontinuity is shown in Figure 14 for the two largest initial opening heights. While for $h_0 = 0.5$ mm the velocity profile closely resembles a parabola, this no longer holds for $h_0 = 5$ mm. These profiles show a clear influence of the fluid inertia, and rather tend to a square shape. Evidently, a much finer discretisation is required to accurately represent this velocity profile with the steep gradients near the fracture walls.

The effect of the initial opening height on the fracture propagation is shown in Figure 15a. While the discontinuity starts to propagate sooner for a larger value of the initial opening height, the difference in

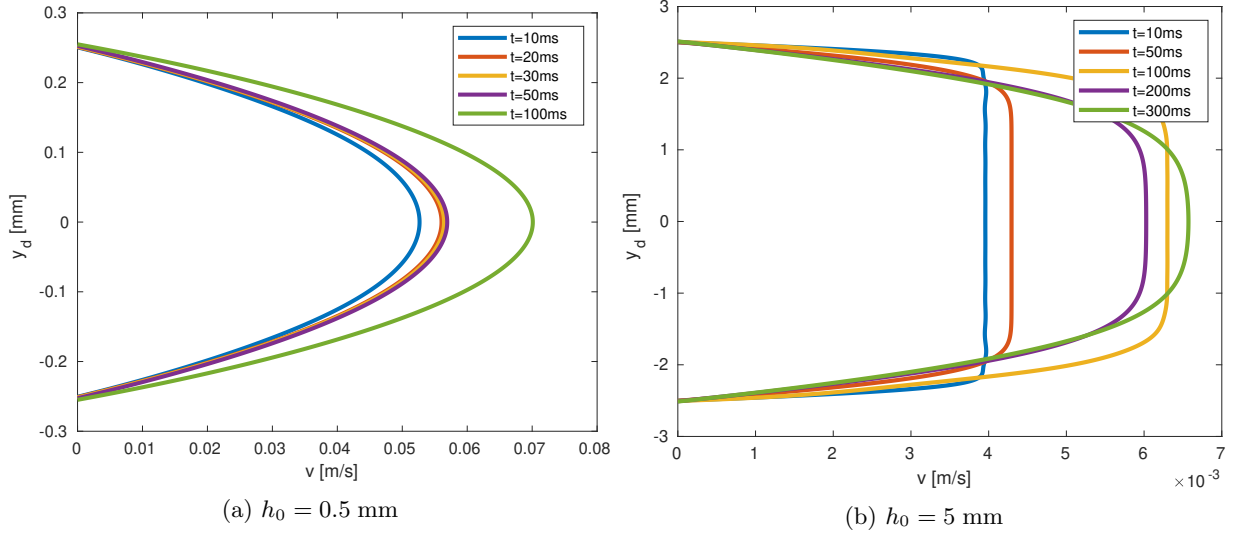


Figure 14: Evolution of the fluid velocity profile at $x = 0.25$ m.

fracture length is small and disappears over time, yielding similar values for the length of the discontinuity for all cases after only 1.5 s. The effect on the inlet pressure, Figure 15b, is larger. In the absence of an initial height, the pressure at the inlet approximates the analytical solution for a simplified problem [63]. The high initial pressure is caused by the high pressure required to open the discontinuity enough to allow the fluid to flow towards the fracture tip. Even though large differences were seen in the velocity profiles between $h_0 = 0.5$ mm and $h_0 = 5$ mm, the differences in the fracture length and in the pressure in the discontinuity are small, indicating that the increased inertial effects for larger opening heights do not alter the fracture propagation, and are limited to the velocity profile within the discontinuity.

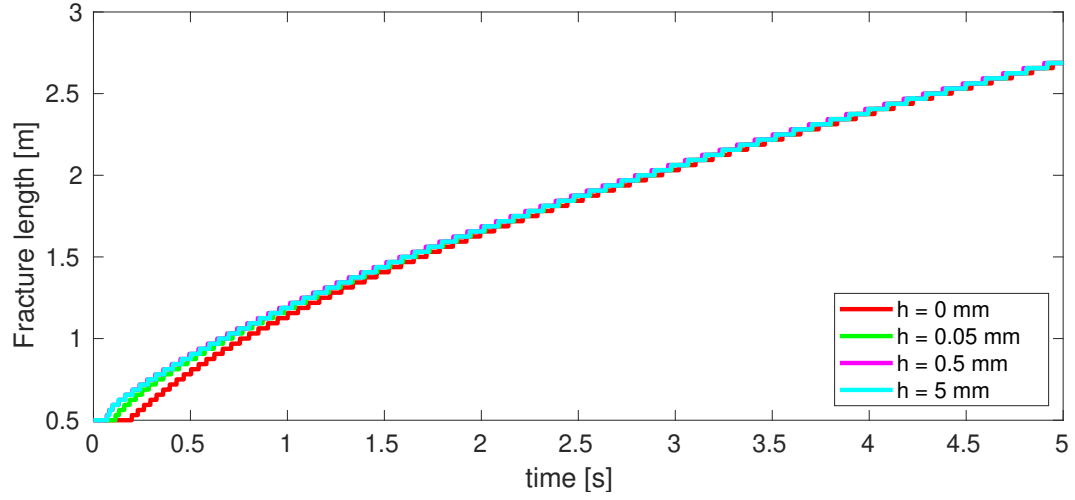
7. Concluding remarks

We have presented a fracture (subgrid) scale model capable of including complex fluid behaviour such as inertial effects and non-Newtonian fluid rheologies without the need to fully discretise and solve for the flow in the interior of the fracture. The velocity profile and the fluid flux are numerically resolving at each integration point at the discontinuity, which is then coupled to the macro-scale equations through the mass conservation at the discontinuity. This allows velocity profiles for which no analytical solution exists to be represented within the framework of a discontinuous pressure model in a crack.

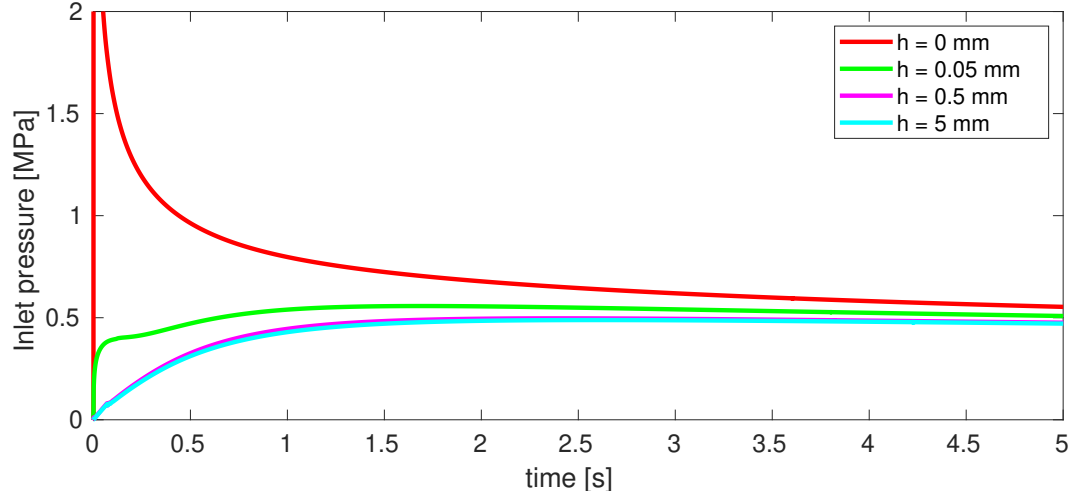
The versatility and possibilities of this fracture scale model have been shown for Newtonian and for Carreau fluids through the simulation of a typical pressurised and propagating fracture. It shows that coarse meshes and large time steps are sufficient to capture the propagation correctly, but that smaller time steps are required to fully resolve the pressure inside the discontinuity. For yet smaller steps, the model is even capable of simulating travelling pressure waves within the discontinuity, indicating that even though the subgrid models in the integration points are solely linked through the gradient of the discontinuity pressure, this is sufficient to properly capture inertial effects.

For the discretisation which is required for the velocity profile in the subgrid model it has been shown that a single quadratic element is sufficient for Newtonian fluids when inertial effects are irrelevant, and only a more refined discretisation is required once inertial effects start to dominate. For Carreau fluids, the same coarse discretisation suffices to resolve the fracture propagation accurately, while a slightly finer discretisation is needed to resolve the velocity profile within the fracture.

Finally, simulations with different initial opening heights have been carried out to assess the relevance of inertial effects. While a clear effect of the fluid inertia on the velocity profile inside the fracture was observed, the effects on the fracture propagation appeared limited. Similarly, increasing the fracture opening height,



(a) Fracture length



(b) Inlet discontinuity pressure

Figure 15: Effect of varying the initial opening height on the fracture length and inlet pressure.

and therefore the fluid inertia, did not significantly alter the pressure at the inlet of the discontinuity. Therefore, for a typical fracture propagation case as presented here, inertial terms alter the velocity profile and are able to cause small duration pressure oscillations, but their effect on the overall fracture propagation is very limited.

Declaration of competing interest

The authors declare that they have no conflict of interest and that the research findings reported here have not been published elsewhere or are under review for another publication.

Acknowledgement Financial support through H2020 European Research Council Advanced Grant 664734 "PoroFrac" is gratefully acknowledged.

Appendix A. Macro-scale discretisation

For the interstitial fluid pressure, the fluid pressure in the discontinuity, and the Cosserat microrotation cubic T-splines are used, while quartic T-splines are used for the displacements to avoid pressure oscillations [64, 65]. Bézier extracted T-splines are used to discretise the pressures and displacements:

$$\mathbf{u} = \sum_{el=1}^{n_{el}} \mathbf{N}_s^{el} \mathbf{u}^{el} \quad p = \sum_{el=1}^{n_{el}} \mathbf{N}_f^{el} p^{el} \quad p_d = \sum_{iel=1}^{n_{iel}} \mathbf{N}_{df}^{iel} p_d^{iel} \quad (\text{A.1})$$

using cubic T-splines \mathbf{N}_f related to the elements for the interstitial pressure. The T-splines \mathbf{N}_{df} are related to the interface elements for the discretisation of the pressure in the discontinuity. The interpolants for the displacements are composed of the quartic T-splines \mathbf{N}_x and \mathbf{N}_y for the displacement and the cubic T-splines \mathbf{N}_ω for the Cosserat rotation:

$$\mathbf{N}_s = \begin{bmatrix} \mathbf{N}_x & \mathbf{0} & \mathbf{0} \\ \mathbf{0} & \mathbf{N}_y & \mathbf{0} \\ \mathbf{0} & \mathbf{0} & \mathbf{N}_\omega \end{bmatrix} \quad (\text{A.2})$$

The time discretisation is performed using a Newmark scheme for the displacements and a θ -scheme for the interstitial pressure and the pressure in the discontinuity:

$$\dot{\mathbf{u}}^{t+\Delta t} = \frac{\gamma}{\beta \Delta t} (\mathbf{u}^{t+\Delta t} - \mathbf{u}^t) - \left(\frac{\gamma}{\beta} - 1 \right) \dot{\mathbf{u}}^t - \left(\frac{\Delta t \gamma}{2\beta} - \Delta t \right) \ddot{\mathbf{u}}^t \quad (\text{A.3})$$

$$\ddot{\mathbf{u}}^{t+\Delta t} = \frac{1}{\beta \Delta t^2} (\mathbf{u}^{t+\Delta t} - \mathbf{u}^t) - \frac{1}{\beta \Delta t} \dot{\mathbf{u}}^t - \left(\frac{1}{2\beta} - 1 \right) \ddot{\mathbf{u}}^t \quad (\text{A.4})$$

$$\dot{p}^{t+\Delta t} = \frac{1}{\theta \Delta t} (p^{t+\Delta t} - p^t) + \left(1 - \frac{1}{\theta} \right) \dot{p}^t \quad (\text{A.5})$$

$$\dot{p}_d^{t+\Delta t} = \frac{1}{\theta \Delta t} (p_d^{t+\Delta t} - p_d^t) + \left(1 - \frac{1}{\theta} \right) \dot{p}_d^t \quad (\text{A.6})$$

Using these discretisations, the momentum balance from Eq. (1) becomes:

$$\mathbf{f}_{ext} - \mathbf{f}_{int} - \mathbf{f}_d = \mathbf{0} \quad (\text{A.7})$$

with the external force vector defined in a standard manner as:

$$\mathbf{f}_{ext} = \int_{\Gamma_t} \mathbf{N}_s^T \bar{\boldsymbol{\tau}} d\Gamma \quad (\text{A.8})$$

and $\bar{\boldsymbol{\tau}}$ the external traction imposed on the boundary of the domain. The internal force vector is given by:

$$\begin{aligned} \mathbf{f}_{int} = & \int_{\Omega} \mathbf{B}^T \boldsymbol{\sigma}_s^{t+\Delta t} - \alpha \mathbf{B}^T \mathbf{m} \mathbf{N}_f p^{t+\Delta t} d\Omega + \int_{\Omega} \mathbf{N}_s^T \bar{\boldsymbol{\rho}} \mathbf{N}_s \left(\frac{1}{\beta \Delta t^2} (\mathbf{u}^{t+\Delta t} - \mathbf{u}^t) - \frac{1}{\beta \Delta t} \dot{\mathbf{u}}^t - \left(\frac{1}{2\beta} - 1 \right) \ddot{\mathbf{u}}^t \right) d\Omega \\ & + \int_{\Omega} \mathbf{N}_s^T \boldsymbol{\rho}_f \mathbf{I}_c^T \left(\frac{1}{\theta \Delta t} (\mathbf{q}^{t+\Delta t} - \mathbf{q}^t) + \left(1 - \frac{1}{\theta} \right) \dot{\mathbf{q}}^t \right) d\Omega \end{aligned} \quad (\text{A.9})$$

using $\mathbf{B} = \mathbf{L} \mathbf{N}_s$ and the fluid flux in the integration points given by:

$$\begin{aligned} \mathbf{q}^{t+\Delta t} = & \left(1 + \frac{\rho_f k}{n_f \mu \theta \Delta t} \right)^{-1} \left(-\frac{k}{\mu} \nabla \mathbf{N}_f p^{t+\Delta t} - \frac{k \rho_f}{\mu} \mathbf{I}_c \mathbf{N}_s \left(\frac{1}{\beta \Delta t^2} (\mathbf{u}^{t+\Delta t} - \mathbf{u}^t) - \frac{1}{\beta \Delta t} \dot{\mathbf{u}}^t - \left(\frac{1}{2\beta} - 1 \right) \ddot{\mathbf{u}}^t \right) \right. \\ & \left. - \frac{k \rho_f}{\mu n_f} \left(\left(1 - \frac{1}{\theta} \right) \dot{\mathbf{q}}^t - \frac{1}{\theta \Delta t} \mathbf{q}^t \right) \right) \end{aligned} \quad (\text{A.10})$$

Finally, the forces related to the discontinuity are obtained from:

$$\mathbf{f}_d = \int_{\Gamma_d} \mathbf{N}_s^T \mathbf{R}^T (\boldsymbol{\tau}_d)^{t+\Delta t} d\Gamma_d \quad (\text{A.11})$$

with \mathbf{R} the rotation matrix at the discontinuity.

The mass balance from Eq. (2) is discretised as:

$$\mathbf{q}_{ext} - \mathbf{q}_{int} - \mathbf{q}_d = \mathbf{0} \quad (\text{A.12})$$

with the external fluxes defined as:

$$\mathbf{q}_{ext} = \Delta t \int_{\Gamma_q} \mathbf{N}_f^T \bar{q} d\Gamma \quad (\text{A.13})$$

using the fluid flux imposed on the boundary \bar{q} . The internal flux vector is given as:

$$\begin{aligned} \mathbf{q}_{int} = & - \int_{\Omega} \frac{1}{M} \mathbf{N}_f^T \mathbf{N}_f \left(\frac{1}{\theta} (\mathbf{p}^{t+\Delta t} - \mathbf{p}^t) + \Delta t \left(1 - \frac{1}{\theta} \right) \dot{\mathbf{p}}^t \right) d\Omega \\ & - \int_{\Omega} \alpha \mathbf{N}_f^T \mathbf{I}_c \mathbf{B} \left(\frac{\gamma}{\beta} (\mathbf{u}^{t+\Delta t} - \mathbf{u}^t) - \Delta t \left(\frac{\gamma}{\beta} - 1 \right) \dot{\mathbf{u}}^t - \Delta t^2 \left(\frac{\gamma}{2\beta} - 1 \right) \ddot{\mathbf{u}}^t \right) d\Omega \\ & + \int_{\Omega} \Delta t (\nabla \mathbf{N}_f)^T \mathbf{q}^{t+\Delta t} d\Omega \end{aligned} \quad (\text{A.14})$$

with the fluid flux in the integration points again obtained from Eq. (A.10). The fluxes due to the discontinuity are given as:

$$\mathbf{q}_d = k_i \Delta t \int_{\Gamma_d} \mathbf{N}_f^T (\mathbf{N}_{df} \mathbf{p}_d^{t+\Delta t} - \mathbf{N}_f \mathbf{p}^{t+\Delta t}) d\Gamma \quad (\text{A.15})$$

The mass balance for the discontinuity, which is resolved for all interface elements, is given as:

$$\mathbf{q}_{d,ext} - \mathbf{q}_{d,int} - \mathbf{q}_{sg} = \mathbf{0} \quad (\text{A.16})$$

using the external flux vector:

$$\mathbf{q}_{d,ext} = \int_{\partial\Gamma_d} \mathbf{N}_{df}^T Q_{tip} d\partial\Gamma \quad (\text{A.17})$$

with the fluid flux imposed at the fracture tips Q_{tip} . The internal fluid flux vector is given by

$$\begin{aligned} \mathbf{q}_{d,int} = & \int_{\Gamma_d} k_i \mathbf{N}_{df}^T \left(\mathbf{N}_f \mathbf{p}^{t+\Delta t} + \mathbf{N}_f \mathbf{p}^{-t+\Delta t} - 2 \mathbf{N}_{df} \mathbf{p}_d^{t+\Delta t} \right) d\Gamma \\ & - \int_{\Gamma_d} \frac{h_0 + \mathbf{n}_d^T \mathbf{N}_{ds} \mathbf{u}^{t+\Delta t}}{K_f} \mathbf{N}_{df}^T \mathbf{N}_{df} \left(\frac{1}{\theta \Delta t} (p_d^{t+\Delta t} - p_d^t) + \left(1 - \frac{1}{\theta} \right) \dot{p}_d^t \right) d\Gamma \\ & + \int_{\Gamma_d} \mathbf{N}_{df}^T \mathbf{n}_d^T \mathbf{N}_{ds} \left(\frac{\gamma}{\beta \Delta t} (\mathbf{u}^{t+\Delta t} - \mathbf{u}^t) - \left(\frac{\gamma}{\beta} - 1 \right) \dot{\mathbf{u}}^t - \left(\frac{\Delta t \gamma}{2\beta} - \Delta t \right) \ddot{\mathbf{u}}^t \right) d\Gamma \end{aligned} \quad (\text{A.18})$$

with the matrix \mathbf{N}_{ds} defined such that $[\![\mathbf{u}]\!] = \mathbf{N}_{ds} \mathbf{u}$. Finally, the fluid flux vector coupling the large scale interface elements to the small scale fracture flow model is given by:

$$\mathbf{q}_{sg} = \int_{\Gamma_d} (\nabla \mathbf{N}_{df})^T q_x^{t+\Delta t} d\Gamma \quad (\text{A.19})$$

with the fluid flux inside the fracture q_x determined at the integration points through the fracture scale model.

Equations (A.7), (A.12) and (A.16) are resolved in a single monolithic scheme. Due to the nonlinearity of the fracture flow an iterative Newton-Raphson method is used to obtain converged pressures and displacements at the new time. To obtain a well-converging scheme, it is important to use correct tangential matrices

to perform the iterations [58]. These matrices are straightforward for the interior of the porous material. However, the matrices for the mass balance from Eq. (A.16) are less trivial due to their dependence on the fracture scale flow model in Eq. A.19 . They are given by:

$$\frac{\partial \mathbf{q}_{sg}}{\partial \mathbf{p}_d} = \int_{\Gamma_d} (\nabla \mathbf{N}_{df})^T \frac{\partial q_x^{t+\Delta t}}{\partial \frac{\partial p_d}{\partial x_d}} \nabla \mathbf{N}_{df} d\Gamma \quad (\text{A.20})$$

$$\frac{\partial \mathbf{q}_{sg}}{\partial \mathbf{u}} = \int_{\Gamma_d} (\nabla \mathbf{N}_{df})^T \frac{\partial q_x^{t+\Delta t}}{\partial h} \mathbf{n}_d^T \mathbf{N}_{ds} d\Gamma \quad (\text{A.21})$$

Therefore, for a subgrid model for the fracture fluid flux to be fully incorporated into the monolithic scheme it not only needs to provide q_x , but also (an approximation of) its derivative with regards to the pressure gradient and the fracture opening height in all integration points of the interface elements.

285 Appendix A.1. Non-Newtonian fluid flux

The equivalent of Eq. A.10, the discretised fluid flux inside the porous material, is given for a Carreau fluid as:

$$\begin{aligned} -\nabla \mathbf{N}_f \mathbf{p}^{t+\Delta t} - \rho_f \mathbf{I}_c \mathbf{N}_s \left(\frac{1}{\beta \Delta t^2} (\mathbf{u}^{t+\Delta t} - \mathbf{u}^t) - \frac{1}{\beta \Delta t} \dot{\mathbf{u}}^t - \left(\frac{1}{2\beta} - 1 \right) \ddot{\mathbf{u}}^t \right) + \frac{\rho_f}{n_f \theta \Delta t} \mathbf{q}^t - \frac{\rho_f}{n_f} \left(1 - \frac{1}{\theta} \right) \dot{\mathbf{q}}^t \\ = \left(\frac{\mu_0 - \mu_\infty}{k} \left(1 + \frac{a_c^2}{c^2 k} (\mathbf{q}^{t+\Delta t})^T \mathbf{q}^{t+\Delta t} \right)^{\frac{n-1}{2}} + \frac{\mu_\infty}{k} + \frac{\rho_f}{n_f \theta \Delta t} \right) \mathbf{q}^{t+\Delta t} \end{aligned} \quad (\text{A.22})$$

This equation for the fluid flux is non-linear, and is therefore solved iteratively for each integration point inside the porous material:

$$\frac{\partial RHS}{\partial \mathbf{q}^{t+\Delta t}} \Delta \mathbf{q}_j^{t+\Delta t} = LHS - RHS_j \quad (\text{A.23})$$

using the definitions:

$$LHS = -\nabla \mathbf{N}_f \mathbf{p}^{t+\Delta t} - \rho_f \mathbf{I}_c \mathbf{N}_s \left(\frac{1}{\beta \Delta t^2} (\mathbf{u}^{t+\Delta t} - \mathbf{u}^t) - \frac{1}{\beta \Delta t} \dot{\mathbf{u}}^t - \left(\frac{1}{2\beta} - 1 \right) \ddot{\mathbf{u}}^t \right) + \frac{\rho_f}{n_f \theta \Delta t} \mathbf{q}^t - \frac{\rho_f}{n_f} \left(1 - \frac{1}{\theta} \right) \dot{\mathbf{q}}^t \quad (\text{A.24})$$

$$RHS_j = \left(\frac{\mu_0 - \mu_\infty}{k} \left(1 + \frac{a_c^2}{c^2 k} (\mathbf{q}_j^{t+\Delta t})^T \mathbf{q}_j^{t+\Delta t} \right)^{\frac{n-1}{2}} + \frac{\mu_\infty}{k} + \frac{\rho_f}{n_f \theta \Delta t} \right) \mathbf{q}_j^{t+\Delta t} \quad (\text{A.25})$$

$$\begin{aligned} \frac{\partial RHS}{\partial \mathbf{q}^{t+\Delta t}} = \left(\frac{\mu_0 - \mu_\infty}{k} \left(1 + \frac{a_c^2}{c^2 k} (\mathbf{q}_j^{t+\Delta t})^T \mathbf{q}_j^{t+\Delta t} \right)^{\frac{n-1}{2}} + \frac{\mu_\infty}{k} + \frac{\rho_f}{n_f \theta \Delta t} \right) \mathbf{I}_2 \\ + (n-1) \frac{a_c^2}{c^2 k} \frac{\mu_0 - \mu_\infty}{k} \left(1 + \frac{a_c^2}{c^2 k} (\mathbf{q}_j^{t+\Delta t})^T \mathbf{q}_j^{t+\Delta t} \right)^{\frac{n-3}{2}} \mathbf{q}_j^{t+\Delta t} \mathbf{q}_j^{t+\Delta t T} \end{aligned} \quad (\text{A.26})$$

with \mathbf{I}_2 the 2×2 identity matrix, $\Delta \mathbf{q}_j^{t+\Delta t}$ the fluid flux update increment (added after each iteration), and the initial guess $\mathbf{q}_0^{t+\Delta t}$ based on the previous fluid flux in the integration point. The converged fluid fluxes in the integration points are used to construct the internal force and flux vectors, Eqs. (A.9) and (A.14). The derivatives required to consistently include this fluid flux into the global Newton-Raphson solver are

given by:

$$\frac{\partial \mathbf{q}^{t+\Delta t}}{\partial p^{t+\Delta t}} = \left(\frac{\partial RHS}{\partial \mathbf{q}^{t+\Delta t}} \right)^{-1} (-\nabla \mathbf{N}_f) \quad (\text{A.27})$$

$$\frac{\partial \mathbf{q}^{t+\Delta t}}{\partial \mathbf{u}^{t+\Delta t}} = \left(\frac{\partial RHS}{\partial \mathbf{q}^{t+\Delta t}} \right)^{-1} \left(-\frac{\rho_f}{\beta \Delta t^2} \mathbf{I}_c \mathbf{N}_s \right) \quad (\text{A.28})$$

using the new fluid flux in the integration points to obtain $\partial RHS / \partial \mathbf{q}^{t+\Delta t}$.

References

- [1] T. Hageman, R. Borst, Stick-slip like behavior in shear fracture propagation including the effect of fluid flow, *International Journal for Numerical and Analytical Methods in Geomechanics* 45 (2021) 965–989.
- [2] S. Secchi, L. Simoni, B. A. Schrefler, Mesh adaptation and transfer schemes for discrete fracture propagation in porous materials, *International Journal for Numerical and Analytical Methods in Geomechanics* 31 (2007) 331–345.
- [3] S. Secchi, B. A. Schrefler, Hydraulic fracturing and its peculiarities, *Asia Pacific Journal on Computational Engineering* 1 (2014) 8.
- [4] T. D. Cao, E. Milanese, E. W. Remij, P. Rizzato, J. J. Remmers, L. Simoni, J. M. Huyghe, F. Hussain, B. A. Schrefler, Interaction between crack tip advancement and fluid flow in fracturing saturated porous media, *Mechanics Research Communications* 80 (2017) 24–37.
- [5] C. Peruzzo, D. T. Cao, E. Milanese, P. Favia, F. Pesavento, F. Hussain, B. A. Schrefler, Dynamics of fracturing saturated porous media and self-organization of rupture, *European Journal of Mechanics - A/Solids* 74 (2019) 471–484.
- [6] F. Pizzoccolo, J. M. Huyghe, K. Ito, Mode I crack propagation in hydrogels is step wise, *Engineering Fracture Mechanics* 97 (2013) 72–79.
- [7] C. Peruzzo, L. Simoni, B. A. Schrefler, On stepwise advancement of fractures and pressure oscillations in saturated porous media, *Engineering Fracture Mechanics* 215 (2019) 246–250.
- [8] R. de Borst, Fluid flow in fractured and fracturing porous media: A unified view, *Mechanics Research Communications* 80 (2017) 47–57.
- [9] I. Berre, F. Doster, E. Keilegavlen, Flow in fractured porous media: A review of conceptual models and discretization approaches, *Transport in Porous Media* 130 (2019) 215–236.
- [10] T. J. Boone, A. R. Ingraffea, A numerical procedure for simulation of hydraulically-driven fracture propagation in poroelastic media, *International Journal for Numerical and Analytical Methods in Geomechanics* 14 (1990) 27–47.
- [11] V. Girault, M. F. Wheeler, B. Ganis, M. E. Mear, A lubrication fracture model in a poro-elastic medium, *Mathematical Models and Methods in Applied Sciences* 25 (2015) 587–645.
- [12] J. M. Segura, I. Carol, Coupled HM analysis using zero-thickness interface elements with double nodes. Part I: Theoretical model, *International Journal for Numerical and Analytical Methods in Geomechanics* 32 (2008) 2083–2101.
- [13] A. R. Khoei, M. Vahab, E. Haghighat, S. Moallemi, A mesh-independent finite element formulation for modeling crack growth in saturated porous media based on an enriched-FEM technique, *International Journal of Fracture* 188 (2014) 79–108.
- [14] M. R. Hirmand, M. Vahab, K. D. Papoulia, N. Khalili, Robust simulation of dynamic fluid-driven fracture in naturally fractured impermeable media, *Computer Methods in Applied Mechanics and Engineering* 357 (2019) 112574.
- [15] A. P. Bunger, E. Detournay, D. I. Garagash, Toughness-dominated hydraulic fracture with leak-off, *International Journal of Fracture* 134 (2005) 175–190.
- [16] E. Chekhonin, K. Levonyan, Hydraulic fracture propagation in highly permeable formations, with applications to tip screenout, *International Journal of Rock Mechanics and Mining Sciences* 50 (2012) 19–28.
- [17] B. Ganis, M. E. Mear, A. Sakhaee-Pour, M. F. Wheeler, T. Wick, Modeling fluid injection in fractures with a reservoir simulator coupled to a boundary element method, *Computational Geosciences* 18 (2014) 613–624.
- [18] S. Lee, M. F. Wheeler, T. Wick, Pressure and fluid-driven fracture propagation in porous media using an adaptive finite element phase field model, *Computer Methods in Applied Mechanics and Engineering* 305 (2016) 111–132.
- [19] C. J. van Duijn, A. Mikelić, T. Wick, A monolithic phase-field model of a fluid-driven fracture in a nonlinear poroelastic medium, *Mathematics and Mechanics of Solids* 24 (2019) 1530–1555.
- [20] E. Gordeliy, A. Peirce, Coupling schemes for modeling hydraulic fracture propagation using the XFEM, *Computer Methods in Applied Mechanics and Engineering* 253 (2013) 305–322.
- [21] T. Mohammadnejad, A. R. Khoei, An extended finite element method for hydraulic fracture propagation in deformable porous media with the cohesive crack model, *Finite Elements in Analysis and Design* 73 (2013) 77–95.
- [22] H. Hajibeygi, D. Karvounis, P. Jenny, A hierarchical fracture model for the iterative multiscale finite volume method, *Journal of Computational Physics* 230 (2011) 8729–8743.
- [23] C. Miehe, S. Mauthe, Phase field modeling of fracture in multi-physics problems. Part III. Crack driving forces in hydro-poro-elasticity and hydraulic fracturing of fluid-saturated porous media, *Computer Methods in Applied Mechanics and Engineering* 304 (2016) 619–655.
- [24] B. Flemisch, I. Berre, W. Boon, A. Fumagalli, N. Schwenck, A. Scotti, I. Stefansson, A. Tatomir, Benchmarks for single-phase flow in fractured porous media, *Advances in Water Resources* 111 (2018) 239–258.

- [25] I. Y. Akkutlu, Y. Efendiev, M. Vasilyeva, Y. Wang, Multiscale model reduction for shale gas transport in poroelastic fractured media, *Journal of Computational Physics* 353 (2018) 356–376.
- [26] J. Réthoré, R. de Borst, M.-A. Abellan, A two-scale approach for fluid flow in fractured porous media, *International Journal for Numerical Methods in Engineering* 71 (2006) 780–800.
- [27] B. Carrier, S. Granet, Numerical modeling of hydraulic fracture problem in permeable medium using cohesive zone model, *Engineering Fracture Mechanics* 79 (2012) 312–328.
- [28] R. de Borst, J. Réthoré, M.-A. Abellan, A numerical approach for arbitrary cracks in a fluid-saturated medium, *Archive of Applied Mechanics* 75 (2006) 595–606.
- [29] E. W. Remij, J. J. C. Remmers, J. M. Huyghe, D. M. J. Smeulders, The enhanced local pressure model for the accurate analysis of fluid pressure driven fracture in porous materials, *Computer Methods in Applied Mechanics and Engineering* 286 (2015) 293–312.
- [30] T. Hageman, R. de Borst, Flow of non-Newtonian fluids in fractured porous media: Isogeometric vs standard finite element discretisation, *International Journal for Numerical and Analytical Methods in Geomechanics* 43 (2019) 2020–2037.
- [31] T. Hageman, K. M. Pervaiz Fathima, R. de Borst, Isogeometric analysis of fracture propagation in saturated porous media due to a pressurised non-Newtonian fluid, *Computers and Geotechnics* 112 (2019) 272–283.
- [32] J. Réthoré, R. de Borst, M.-A. Abellan, A two-scale model for fluid flow in an unsaturated porous medium with cohesive cracks, *Computational Mechanics* 42 (2008) 227–238.
- [33] T. Hageman, R. de Borst, Sub-grid models for multiphase fluid flow inside fractures in poroelastic media, *Journal of Computational Physics* 414 (2020) 109481.
- [34] E. A. Bergkamp, C. V. Verhoosel, J. J. C. Remmers, D. M. J. Smeulders, A staggered finite element procedure for the coupled Stokes-Biot system with fluid entry resistance, *Computational Geosciences* 24 (2020) 1497–1522.
- [35] I. Ambartsumyan, E. Khattatov, I. Yotov, P. Zunino, A Lagrange multiplier method for a Stokes–Biot fluid–poroelastic structure interaction model, *Numerische Mathematik* 140 (2018) 513–553.
- [36] I. Ambartsumyan, E. Khattatov, T. Nguyen, I. Yotov, Flow and transport in fractured poroelastic media, *GEM - International Journal on Geomathematics* 10 (2019) 1–34.
- [37] L. Mu, J. Wang, X. Ye, A stable numerical algorithm for the Brinkman equations by weak Galerkin finite element methods, *Journal of Computational Physics* 273 (2014) 327–342.
- [38] S. Caucao, G. N. Gatica, R. Oyarzúa, N. Sánchez, A fully-mixed formulation for the steady double-diffusive convection system based upon Brinkman–Forchheimer equations, *Journal of Scientific Computing* 85 (2020) 44.
- [39] E. Cosserat, F. Cosserat, *Théorie des Corps Déformables*, A. Hermann & Fils, Paris, 1909.
- [40] R. de Borst, L. J. Sluys, Localisation in a Cosserat continuum under static and dynamic loading conditions, *Computer Methods in Applied Mechanics and Engineering* 90 (1991) 805–827.
- [41] R. de Borst, Simulation of strain localization: A reappraisal of the Cosserat continuum, *Engineering Computations* 8 (1991) 317–332.
- [42] T. Hageman, S. A. Sabet, R. de Borst, Convergence in non-associated plasticity and fracture propagation for standard, rate-dependent, and Cosserat continua, *International Journal for Numerical Methods in Engineering*
- [43] O. C. Zienkiewicz, A. H. C. Chan, M. Paston, B. A. Schrefler, T. Shiomi, *Computational Geomechanics – With Special Reference to Earthquake Engineering*, John Wiley & Sons, Chichester, 1999.
- [44] R. de Borst, *Computational Methods for Fracture in Porous Media*, Elsevier, New York, 2017.
- [45] K. M. Pervaiz Fathima, R. de Borst, Implications of single or multiple pressure degrees of freedom at fractures in fluid-saturated porous media, *Engineering Fracture Mechanics* 213 (2019) 1–20.
- [46] T. P. Y. Lhomme, Initiation of Hydraulic Fractures in Natural Sandstone, Ph.D. thesis, TU Delft, Delft (2005).
- [47] B. A. Schrefler, S. Secchi, L. Simoni, On adaptive refinement techniques in multi-field problems including cohesive fracture, *Computer Methods in Applied Mechanics and Engineering* 195 (2006) 444–461.
- [48] S. Lee, M. F. Wheeler, T. Wick, Pressure and fluid-driven fracture propagation in porous media using an adaptive finite element phase field model, *Computer Methods in Applied Mechanics and Engineering* 305 (2016) 111–132.
- [49] T. Ni, F. Pesavento, M. Zaccariotto, U. Galvanetto, Q. Z. Zhu, B. A. Schrefler, Hybrid FEM and peridynamic simulation of hydraulic fracture propagation in saturated porous media, *Computer Methods in Applied Mechanics and Engineering* 366 (2020) 113101.
- [50] Y. Bazilevs, V. M. Calo, J. A. Cottrell, J. A. Evans, T. J. R. Hughes, S. Lipton, M. A. Scott, T. W. Sederberg, Isogeometric analysis using T-splines, *Computer Methods in Applied Mechanics and Engineering* 199 (2010) 229–263.
- [51] M. A. Scott, X. Li, T. W. Sederberg, T. J. R. Hughes, Local refinement of analysis-suitable T-splines, *Computer Methods in Applied Mechanics and Engineering* 213–216 (2012) 206–222.
- [52] M. A. Scott, M. J. Borden, C. V. Verhoosel, T. W. Sederberg, T. J. R. Hughes, Isogeometric finite element data structures based on Bézier extraction of T-splines, *International Journal for Numerical Methods in Engineering* 88 (2011) 126–156.
- [53] S. May, J. Vignollet, R. de Borst, The role of the Bézier extraction operator for T-splines of arbitrary degree: linear dependencies, partition of unity property, nesting behaviour and local refinement, *International Journal for Numerical Methods in Engineering* 103 (2015) 547–581.
- [54] C. V. Verhoosel, M. A. Scott, R. de Borst, T. J. R. Hughes, An isogeometric approach to cohesive zone modeling, *International Journal for Numerical Methods in Engineering* 87 (2011) 336–360.
- [55] L. Chen, R. de Borst, Locally refined T-splines, *International Journal for Numerical Methods in Engineering* 114 (2018) 637–659.
- [56] L. Chen, C. V. Verhoosel, R. de Borst, Discrete fracture analysis using locally refined T-splines, *International Journal for Numerical Methods in Engineering* 116 (2018) 117–140.
- [57] J. Vignollet, S. May, R. de Borst, Isogeometric analysis of fluid-saturated porous media including flow in the cracks,

- International Journal for Numerical Methods in Engineering 108 (2016) 990–1006.
- 405 [58] T. Hageman, R. de Borst, A convergence study of monolithic simulations of flow and deformation in fractured poroelastic media, International Journal for Numerical Methods in Engineering 121 (2020) 393–410.
- [59] P. J. Carreau, Rheological equations from molecular network theories, Transactions of the Society of Rheology 16 (1972) 99–127.
- 410 [60] J. R. A. Pearson, P. M. J. Tardy, Models for flow of non-Newtonian and complex fluids through porous media, Journal of Non-Newtonian Fluid Mechanics 102 (2002) 447–473.
- [61] V. J. Ervin, E. W. Jenkins, S. Sun, Coupled generalized nonlinear Stokes flow with flow through a porous medium, SIAM Journal on Numerical Analysis 47 (2009) 929–952.
- [62] S. Müntenmaier, First-Order system least squares for generalized-Newtonian coupled Stokes-Darcy flow, Numerical Methods for Partial Differential Equations 31 (2015) 1150–1173.
- 415 [63] D. A. Spence, P. Sharp, Self-similar solutions for elastohydrodynamic cavity flow, Proceedings of the Royal Society of London. A. Mathematical and Physical Sciences 400 (1985) 289–313.
- [64] F. Brezzi, M. Fortin, Mixed and Hybrid Finite Element Methods, Vol. 15 of Springer Series in Computational Mathematics, Springer, New York, NY, 1991.
- [65] D. Chapelle, K. J. Bathe, The inf-sup test, Computers & Structures 47 (1993) 537–545.